

Two-temperature accretion flows around strongly magnetized stars and their spectral analysis

Shilpa Sarkar,^{1,2,5}★ Kuldeep Singh,¹ Indranil Chattopadhyay¹† and Philippe Laurent^{3,4}

¹Aryabhata Research Institute of Observational Sciences (ARIES), Manora Peak, Nainital, Uttarakhand 263002, India

²Pt. Ravishankar Shukla University, Great Eastern Rd, Amanaka, Raipur, Chhattisgarh 492010, India

³IRFU / Service d'Astrophysique, Bat. 709 Orme des Merisiers, CEA Saclay, 91191 Gif-sur-Yvette, Cedex France

⁴Laboratoire Astroparticule et Cosmologie, Bâtiment Condorcet, 10, rue Alice Domont et Léonie Duquet, 75205 Paris, Cedex France

⁵IUCAA, Ganeshkhind, Pune 411007, India

Accepted XXX. Received YYY; in original form ZZZ

ABSTRACT

We investigate two-temperature accretion flows onto strongly magnetized compact stars. Matter is accreted in the form of an accretion disc upto the disc radius (r_d), where, the magnetic pressure exceeds both the gas and ram pressure and thereafter the matter is channelled along the field lines onto the poles. We solve the equations of motion self-consistently along the field lines, incorporating radiative processes like bremsstrahlung, synchrotron and inverse-Comptonization. For a given set of constants of motion, the equations of motion do not produce unique transonic solution. Following the second law of thermodynamics the solution with the highest entropy is selected and thereby eliminating the degeneracy in solution. We study the properties of these solutions and obtain corresponding spectra as a function of the magnetic field (B_*), spin period (P) and accretion rate of the star (\dot{M}). A primary shock is always formed just near the surface. The enhanced radiative processes in this post-shock region slows down the matter and it finally settles on the surface of the star. This post-shock region contributes to $\gtrsim 99.99\%$ of the total luminosity obtained from the accretion flow. It is still important to study the full accretion flow because secondary shocks may be present for some combination of B_* , P and \dot{M} in addition to primary shocks. We find that secondary shocks, if present, produce an extended emission at higher energies in the spectra.

Key words: stars – accretion flows – shocks – magnetic fields – spectra

1 INTRODUCTION

Accretion onto magnetized stars remains one of the hot topics of research interest since the discovery of X-ray pulsars (Giacconi et al. 1971). These pulsars were later found to be neutron stars (NSs) accreting matter from their binary counterpart, either via stellar wind or Roche lobe overflow (Pringle & Rees 1972; Davidson & Ostriker 1973; Lamb et al. 1973). The matter accreted generally possess some angular momentum because of which it first forms an accretion disc similar to a black hole (BH) accretion disc. But in the presence of strong magnetic field, accretion disc terminates at some radius called the magnetospheric radius. Thereafter, accretion proceeds along the curved magnetic field lines. Pringle & Rees (1972) suggested that emission would mostly come from a region close to the poles of the star.

Koldoba et al. (2002) studied the behaviour of accretion flow along an aligned dipole magnetic field around rotating magnetized stars (NSs and young stellar objects), *i.e.*, along a curved flow geometry. They utilised the magneto-hydrodynamic (MHD) integrals (Weber & Davis 1967; Mestel 1968; Lovelace et al. 1986) as well as Bernoulli parameter that are conserved along the field lines, to obtain global transonic accretion solution, connecting the accretion disc to the

poles of the star. It is important to note that since stars possess a hard surface, matter accreted should settle down onto the surface of the star (Fukue 1987). This demands the formation of a shock, whereby the kinetic energy of the matter could be radiated away (Li et al. 1996). Koldoba et al. (2002) did not address this issue and considered only adiabatic flows which possessed supersonic velocity near the star's surface. Karino et al. (2008) followed Koldoba et al. and obtained shocked solutions, however the shock obtained was located farther from the star's surface, while it is more likely that the terminating shock for the accretion column should be nearer to the star's surface. Moreover, in their work, even the post-shock flows have relatively higher speeds close to the star's surface, *i.e.*, did not satisfy the star's surface boundary conditions. Since the accretion column is expected to be terminated at a shock close to the surface, thus a large number of works focused just on the region close to the post-shock accretion column, which enabled them to study in detail the emission processes responsible for the observable spectrum (Davidson 1973; Arons et al. 1987; Becker 1998; Becker & Wolff 2005a,b, 2007; Becker et al. 2012; Wolff et al. 2019; Becker & Wolff 2020).

Singh & Chattopadhyay (2018a) followed the methods of Koldoba et al. (2002); Karino et al. (2008) but included cyclotron and bremsstrahlung cooling. They obtained self-consistent magnetized accretion solutions, which connected the flow from the inner region of the accretion disc (r_d) to the star's pole via a surface shock (also known as primary shock, r_{ps}). They discussed the importance of ra-

★ E-mail: shilpa.sarkar30@gmail.com

† E-mail: indra@aries.res.in

diative cooling in the post-shock flow for the matter to slow down with asymptotically zero speed near the star's surface. However, the temperatures of an accretion flow starting from the accretion disc edge to the poles of the star varies by more than 3-4 orders of magnitude. For such a wide variation in temperature, a fixed Γ (i. e., adiabatic index) equation of state (EoS) for the gas is untenable (Taub 1948; Chandrasekhar 1939; Ryu et al. 2006). Singh & Chattopadhyay (2018b) extended their previous work and instead of using a fixed Γ EoS, they now used a variable Γ EoS proposed by Chattopadhyay & Ryu (2009), also known as CR EoS, which is dependent on the temperature as well as the composition of the flow. Singh & Chattopadhyay (2018b) showed that there are multiple sonic point regions in magnetized accretion flows. Therefore, many modes of accretion through the bipolar magnetic field funnels are possible, and not just a column or a conical flow onto an optically thick post-shock region.

Two-temperature accretion flows

Ionized astrophysical plasma is composed of different particles (electrons and protons). If these particles are not given sufficient time to interact within themselves, or technically, if the Coulomb coupling between the species is weak, then this would lead to a two-temperature flow, where protons and electrons would be defined by two different temperature distributions. In most of the astrophysical systems, this condition is found to be valid. The infall timescales are generally very much shorter than the Coulomb coupling timescales (Shapiro et al. 1976; Stepney 1983; Colpi et al. 1984; Park 1990; Yuan & Narayan 2014). In addition, radiation mechanisms acting on electrons and protons are different because of their different masses and scattering cross-sections. Thus, electrons and protons are likely to settle down into two different temperature distributions. A lot of work has been done in two-temperature accretion flows around BHs (Nakamura et al. 1996; Manmoto et al. 1997; Yuan et al. 2003; Mandal & Chakrabarti 2005; Sądowski et al. 2017; Sądowski et al. 2016; Dihingia et al. 2018, 2020; Chael et al. 2019), as well as for flows around magnetized stars (Shapiro & Salpeter 1975; Langer & Rappaport 1982; Narayan & Yi 1995; Saxton et al. 2005; West et al. 2017a,b; Bu et al. 2020; Becker & Wolff 2022).

Liang & Thompson (1980) (hereafter, LT80) identified a problem while solving two-temperature solutions around compact objects. With respect to one-temperature flows, we have an additional variable in two-temperature system which is the extra temperature. To obtain a solution the above authors made an arbitrary assumption. To quote LT80 verbatim “..... because of the uncertainty in the mechanism coupling electrons and ions, we simply parameterize T_p/T_e as a constant”. In other words, it suggests that if the ratio between the temperatures is changed to some other constant value, we would obtain a completely different solution. This indicated that there is a degeneracy present in the two-temperature system unlike in case of one-temperature flows where for a given set of CoM we get a unique transonic solution. This degeneracy is irrespective of the type of central object and is generic to two-temperature flows. Apart from LT80, there are a number of papers indicating the same degeneracy issue. Similar to LT80 where T_p/T_e is parameterized, other works followed some other methodology to constrain the degeneracy. We have grouped them together and have discussed them below. We note that the works discussed below are related to magnetized stars only. *Parameterising of shock jump values:* In 1975, Shapiro & Salpeter studied funnel flows in two temperature regime, but considered only the post-shock region to obtain solutions and compute the spectrum. They considered the ratio between T_p and T_e just after the shock as a parameter (marked as β_s in their paper). Similar approach was

adopted by Saxton et al. (2005) for obtaining two-temperature accretion solutions around white dwarfs and West et al. (2017a,b) used it for NSs.

Assumption of additional relation to determine T_p and T_e : Langer & Rappaport (1982) also considered the post shock accretion column while computing the spectrum. However, they utilised an arbitrary assumption to obtain the value of T_e . They assumed that the heating of electrons by ions (Q_e^+) equals the radiative cooling (Q_e^-). In other words, $Q_e^+ = Q_e^-$. This assumption is arbitrary and need not be true, since some amount of electron heat could be advected inwards with the flow towards the central object (Manmoto et al. 1997, in case of BHs). A similar approach was used by Medvedev & Narayan (2001) where they obtained full global but self-similar solutions around an NS utilising the above assumption with weak magnetic field.

In a series of papers by Sarkar & Chattopadhyay (2019a,b) (hereafter, SC19a; SC19b), Sarkar, Chattopadhyay & Laurent (2020) (hereafter, SCL20) and Sarkar & Chattopadhyay (2022) (hereafter, SC22) which are based on two-temperature accretion flows around BHs, it has been discussed that these flows are degenerate in nature. The reason for this degeneracy is the increase in the number of flow variables (an extra temperature) without any increase in the number of requisite equations. In one-temperature regime, however, this was not the case and for a given set of CoM, a unique transonic solution existed (also, see KSC18a; KSC18b). But in the two-temperature regime, infinite number of transonic solutions were obtained. In the papers SC19a; SC19b; SCL20; SC22, this problem of degeneracy was attended and a novel methodology to constrain it was proposed. Apart from energy and other CoM, fluids are also characterized by entropy. Bondi in 1952 concluded that a transonic solution is the one with maximum entropy and would be preferred by nature. Also, Becker & Le (2003); Becker et al. (2008) used the concept of entropy close to the BH horizon, in addition to other integrals of motion, to obtain a transonic BH accretion solution. Although these works were done in the one-temperature regime, but the concept provided by these authors, that entropy can be used as a tool to chose the correct solution, also served as the basis to remove degeneracy in two-temperature solutions. The integration of the first law of thermodynamics gives the measure of entropy. In two-temperature regime, we have two differential equations for temperature (dT_p/dr and dT_e/dr) coupled by the Coulomb coupling term which inhibits the integration of these equations to obtain an analytical expression of entropy. Fortunately the presence of event horizon in case of BH solves the problem. Utilising the fact that close to the event horizon, gravity overpowers any other interaction or processes and matter velocities approach free-fall velocities, the first law of thermodynamics can be integrated and an expression for entropy is admissible, which is strictly valid near the horizon. Using this entropy measure, SC19a; SC19b; SCL20; SC22 obtained unique two-temperature accretion solutions around BHs.

The situation gets complicated for the case of magnetized stars which possess a hard surface unlike the BH event horizon. Thus the form of entropy measure proposed above cannot be applied in a similar fashion for flows around magnetized stars. Although the gravity of magnetized stars makes the accreting matter supersonic, but the presence of hard surface drives a shock in the accretion column (see also Li et al. 1996), after which the velocity of the matter reduces to negligible values. Even if it is assumed that the supersonic matter directly hits the star's surface (Koldoba et al. 2002) without forming a shock, the matter would still not achieve velocities high enough ($v \approx c$), to use the entropy expression and obtain a measure of entropy close to the surface. This leads to a serious problem of constraining the degeneracy in two-temperature accretion flows around magne-

tized stars. Therefore, in this paper, we propose a novel methodology to remove degeneracy and obtain unique transonic two-temperature accretion solutions around magnetized stars for a given set of CoM. We elaborately discuss it in the methodology section. Thereafter, we investigate accretion solutions for a large set of parameter space, to get a global picture of these accreting systems. In addition, we also perform the spectral analysis.

This paper is arranged according to the following sections. In section 2, we introduce the basic equations and assumptions used and in section 3, we discuss the methodology to obtain a unique transonic two-temperature solution. In section 4, we present and discuss the results obtained for a large set of parameter space. We also present spectral analysis in this section and then conclude in section 5.

2 BASIC EQUATIONS OF MOTION AND ASSUMPTIONS

2.1 MHD equations

The work is done in the ideal MHD regime assuming steady, axisymmetric and inviscid flow (Chandrasekhar 1956; Heinemann & Olbert 1978; Lovelace et al. 1986; Ustyugova et al. 1999) in spherical coordinate system (r, θ, ϕ) . The velocity and magnetic field are given by, $\mathbf{v} = v_{\text{po}} + v_{\phi} \hat{\boldsymbol{\phi}}$ and $\mathbf{B} = B_{\text{po}} + B_{\phi} \hat{\boldsymbol{\phi}}$, respectively. The subscripts ‘po’ and ϕ represents the poloidal and toroidal component respectively and $\hat{\boldsymbol{\phi}}$ is the unit vector. In steady state and under axisymmetry assumption, the basic MHD equations are as follows :

$$\text{Mass conservation equation : } \nabla \cdot (\rho \mathbf{v}) = 0, \quad (1)$$

$$\text{Momentum conservation equation :}$$

$$(\rho \mathbf{v} \cdot \nabla) \mathbf{v} = -\nabla p + \frac{1}{c} (\mathbf{J} \times \mathbf{B}) - \rho \nabla \Phi_{\text{g}}, \quad (2)$$

$$\text{Faraday's law using ideal Ohm's law : } \nabla \times (\mathbf{v} \times \mathbf{B}) = 0, \quad (3)$$

$$\text{Divergence constraint : } \nabla \cdot \mathbf{B} = 0, \quad (4)$$

where, ρ is the mass density, p is the isotropic plasma pressure, c is the speed of light, Φ_{g} is the gravitational potential of the star and \mathbf{J} is the current density which is $(\nabla \times \mathbf{B})/4\pi$ from Ampere's law. In order to mimic the effects of strong gravity we use the Paczyński & Wiita potential (Paczyński & Wiita 1980) throughout this work, which is given by, $\Phi_{\text{g}} = -GM_*/(r - r_{\text{g}})$ where $r_{\text{g}} = 2GM_*/c^2$ is the Schwarzschild radius, G is the gravitational constant and M_* is mass of the star.

Apart from the above equations, we need the first law of thermodynamics to study the temperature variation inside the system in the presence of advection and dissipation, which is given by :

$$\frac{p}{\rho^2} \frac{d\rho}{ds} - \frac{d(e/\rho)}{ds} = \frac{Q^+ - Q^-}{\rho v_{\text{po}}} = \frac{\Delta Q}{\rho v_{\text{po}}}, \quad (5)$$

where, e is the internal energy density, Q^+ and Q^- are the heating and cooling rates, respectively and $\Delta Q = Q^+ - Q^-$. The first law of thermodynamics is written separately for the two different species (protons and electrons), but are coupled by the Coulomb coupling term, which is responsible for energy exchange between the protons and electrons. Detailed discussion regarding the dissipative processes is given in section 2.6.

2.2 MHD integrals

We introduce a flux function $\Psi(r, \theta)$ (Lovelace et al. 1986; Ustyugova et al. 1999; Koldoba et al. 2002; KSC18a; KSC18b), which represents

Table 1. The variables and some abbreviations used in the paper and their description

Variable	Description
v	Flow velocity (subscript $\phi \rightarrow$ toroidal component, po \rightarrow poloidal component)
B	Magnetic field (subscript definition same as v)
ρ	Mass density
Φ	Potentials (subscript g \rightarrow Gravitational potential, centri \rightarrow potential due to centrifugal forces)
p	Pressure
e	internal energy density
Q^+, Q^-	Heating and cooling rates
ds	Differential line element along the field line
$\dot{M}, \dot{M}_{\text{Edd}}$	Accretion rate, Eddington rate
A_{po}	Cross-sectional area perpendicular to B_{po}
$\kappa(\Psi)$	Mass flux to magnetic flux ratio
$\Omega(\Psi)$	Angular velocity of the field lines
ω	Angular velocity of the matter
$L(\Psi)$	Total angular momentum
$E(\Psi)$	Generalised Bernoulli parameter
\mathcal{E}	Canonical form of Bernoulli constant
h	Specific enthalpy
r	Radius in spherical coordinates
θ	Co-latitude of r
Ψ	Stream function or magnetic flux function
μ	Magnetic moment
$r_{\text{d}} = \mu/\Psi$	Disc radius defined as the radius from the center of the star to the point where the field line crosses the equatorial plane of the disc.
r_{co}	Co-rotation radius
α	Ratio between the co-rotation radius and disc radius(= $r_{\text{co}}/r_{\text{d}}$)
n_i	Number density ($i = e, p$ for electrons and protons respectively).
m_i	Mass of i^{th} species
T_i	Temperature of i^{th} species
Θ_i	Dimensionless temperature defined w.r.t the rest mass of the species [= $kT_i/(m_i c^2)$]
Γ_i	Adiabatic index for i^{th} species
N_i	Polytropic index for i^{th} species
ΔQ_i	Difference in the heating and cooling rates (= $Q_i^+ - Q_i^-$)
a_s	Sound speed
M	Mach number (v/a_s)
M_*	Mass of the NS
r_*	Radius of the NS
B_*	Surface magnetic field of the NS
B_{10}	B_* in terms of 10^{10}G
P	Period of the NS
r_{g}	Schwarzschild radius (= $2GM_*/c^2$)
\dot{M}	Entropy accretion rate
r_{in}	A point where the fluid velocity reaches free-fall velocity
Subscript ‘in’	Represents the value of variables ($r, v, n_i, T_i, \Theta_i, f_i, A, \dot{M}, M$) at $r \rightarrow r_{\text{in}}$
$T_{\text{pin max}}$	Proton temperature for maximum entropy solution
CR	Compression ratio at the shock location
Subscript ‘c’	Represents the value of variables (r, v, M, T_i, Θ_i) at the sonic point
$r_{\text{c}}^{\text{in}}, r_{\text{c}}^{\text{mid}}, r_{\text{c}}^{\text{out}}$	Inner, middle and outer sonic points respectively
Subscript ‘ps’	Represents the value of variables (r, CR) at the primary shock location
Subscript ‘ss’	Represents the value of variables (r, CR) at the secondary shock location
EoS	Equation of state
EoM	Equation of motion
CoM	Constant of motion
TS	Transonic Solution

a specific magnetic field line. On integrating the equations numbered (1) to (4), we obtain quantities that remain conserved along these field lines. They are : $\kappa(\Psi)$, $\Omega(\Psi)$, $L(\Psi)$ and $E(\Psi)$ arising due to the conservation of mass, angular velocity of field lines, total angular momentum and energy, respectively. The derivation of these quantities are discussed below.

Integrating continuity equation (1), gives the equation for conservation of mass flux, which is given by,

$$\dot{M} = \rho v_{\text{po}} A_{\text{po}} = \text{constant}, \quad (6)$$

where, \dot{M} is known as the accretion rate of the system. From the Eq. (4), we obtain the magnetic flux conservation,

$$B_{\text{po}} A_{\text{po}} = \text{constant}, \quad (7)$$

where, A_{po} is the cross-sectional area perpendicular to the magnetic field B_{po} . From Eqs. (6) and (7), we obtain a relation between v_{po} , ρ and B_{po} which is given by,

$$v_{\text{po}} = \frac{\kappa(\Psi)}{4\pi\rho} B_{\text{po}}, \quad (8)$$

where, $\kappa(\Psi) = \text{constant}$, is the mass flux to magnetic flux ratio. The poloidal field lines are the streamlines, so a differential element on the field line is

$$ds^2 = dr^2 + r^2 d\theta^2 = dr^2 \left[1 + r^2 \left(\frac{d\theta}{dr} \right)^2 \right]. \quad (9)$$

So, B_{po} and v_{po} are locally tangential to ds .

The Faraday equation (3) gives conservation of the angular velocity $\Omega(\Psi)$ of field lines,

$$\Omega(\Psi) = \omega - \frac{\kappa(\Psi) B_{\phi}}{4\pi\rho\tilde{r}} = \text{constant}, \quad (10)$$

where, $\tilde{r} = r \sin\theta$ and $\omega = v_{\phi}/\tilde{r}$ is the angular velocity of the matter. From the azimuthal component of Euler equation (2), we get the conservation of total angular momentum $L(\Psi)$,

$$L(\Psi) = \omega\tilde{r}^2 - \frac{B_{\phi}\tilde{r}}{\kappa(\Psi)} = \text{constant}. \quad (11)$$

On integrating the poloidal component of the Euler equation (2) with the help of Eqs. (10 & 5), we get the generalized Bernoulli constant or in other words, the total energy E of the flow, which is given by,

$$E(\Psi) = \frac{1}{2}v_{\text{po}}^2 + \frac{1}{2}(\omega - \Omega)^2\tilde{r}^2 + h + \Phi_{\text{g}} - \frac{\Omega^2\tilde{r}^2}{2} + \int \frac{\Delta Q}{\rho v_{\text{po}}} ds = \text{constant}, \quad (12)$$

where, h denotes the enthalpy. The last term arises due to the presence of dissipative processes in the system.

2.3 Stream function and the strong magnetic field assumption

We assume the magnetized star to have dipole-like magnetic field. The magnetic flux function for this field in spherical coordinates is,

$$\Psi = \frac{\mu}{r} \sin^2\theta, \quad (13)$$

and the geometry of the dipole field lines is given by,

$$r = r_{\text{d}}(\Psi) \sin^2\theta, \quad (14)$$

where, r is the spherical radial coordinate, θ is the co-latitude, μ is the magnetic moment and $r_{\text{d}} = \mu/\Psi$ is the radius from the center of the star to the point where the field line (Ψ) crosses the equatorial plane of the disc. In our work, r_{d} is also the radius from where the matter starts

channelling through the magnetic field lines from the accretion disc as shown in Fig. (1). We see from this equation that r and θ are not independent and are constrained through this relation. The poloidal magnetic field considered is dipolar *i.e.*, $\mathbf{B}_{\text{po}} = 3\mathbf{r}(\boldsymbol{\mu} \cdot \mathbf{r})/r^5 - \boldsymbol{\mu}/r^3$ and can be simplified to get (Koldoba et al. 2002; Karino et al. 2008),

$$B_{\text{po}}(r) = \frac{\mu}{r^3} \sqrt{4 - \frac{3r}{r_{\text{d}}}}. \quad (15)$$

We assume the star's rotation axis to be co-aligned with the magnetic moment (μ) $\Rightarrow \Omega \parallel \mu$ (see, Fig. 1). Since our main focus in this work is to find consistent two temperature accretion solution onto magnetised stars (not particularly pulsars), we chose the cases where the magnetic field axis and rotation axis are aligned. Simplified as the case may be, but our analysis captures the qualitative features of these types of flows. Lyne & Manchester (1988) showed that old pulsars have aligned axes and this alignment is achieved in times scales of the order of 10^7 years (Yang & Li 2023; Biryukov & Abolmasov 2021). Even some young pulsars with similar alignment are also reported in literature. The current paper directly applies to these types of system, and we aim to attend the issue of misalignment in some subsequent work. In addition, we assume the star's magnetic field to be strong enough such that the matter flow does not affect the magnetic field geometry. This is valid when the magnetic energy density is much larger than the gas or ram pressures (Koldoba et al. 2002) and can be expressed as,

$$B_{\text{po}}^2/8\pi \gg p, \quad (\rho v_{\text{po}}^2) \quad (16)$$

In the strong magnetic field limit and after some simple calculations we arrive at two main conclusions (for the derivation part see, Koldoba et al. (2002), KSC18a; KSC18b), which can be represented as:

$$|\omega - \Omega| \ll \Omega \quad \text{and} \quad \frac{B_{\phi}}{B_{\text{po}}} \ll 1. \quad (17)$$

The first relation implies that matter moves with the same angular velocity as the field lines. Additionally since these field lines are strongly anchored to the surface of the star, they rotate with the same angular velocity as that of the star, or $\Omega_{\text{matter}} = \Omega(\Psi) = \Omega_{\text{star}} = \Omega$. This also implies that r_{d} is very close to the co-rotation radius (r_{co}) or $r_{\text{d}} \simeq r_{\text{co}}$. Second relation dictates that it is safe to ignore the toroidal component of the magnetic field which is negligibly small compared to its poloidal component.

The effective potential of an accretion flow along a given field line $\Psi(r, \theta) = \text{constant}$, in a reference frame co-rotating with the star can be represented as the sum of the gravitational and centrifugal forces,

$$\Phi(r) = \Phi_{\text{g}} + \Phi_{\text{centri}} = -\frac{GM_*}{r - r_{\text{g}}} - \frac{\Omega^2 r^2 \sin^2\theta}{2}. \quad (18)$$

On simplifying the above equation using the definition of r_{d} from Eq. (14) and the relations $r_{\text{co}} \equiv (GM_*/\Omega^2)^{1/3}$ and $\alpha \equiv r_{\text{co}}/r_{\text{d}}$, we get,

$$\Phi(r) = -\Omega^2 r_{\text{co}}^2 \left[\frac{\alpha r_{\text{d}}}{r - r_{\text{g}}} + \frac{(r/r_{\text{d}})^3}{2\alpha^2} \right]. \quad (19)$$

Now imposing the strong magnetic field condition (Eqs. 17) and using Eq. (19), we simplify the generalised Bernoulli constant defined along a specific stream line $\Psi(r, \theta) = \text{constant}$, given in Eq. (12) to,

$$E(\Psi) = \frac{1}{2}v_{\text{po}}^2 + h + \Phi(r) + \int \frac{\Delta Q}{\rho v_{\text{po}}} ds. \quad (20)$$

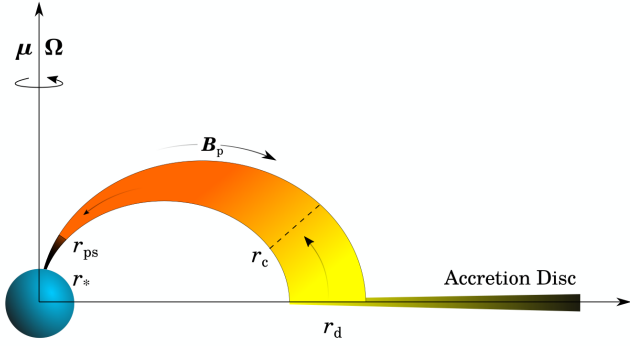


Figure 1. Representation of a magnetized accretion flow. The disc radius is marked as r_d , sonic point as r_c , primary shock as r_{ps} and r_* is the radius of the star.

In the above equation and in the rest of the paper, we have considered $\alpha = 1$. This expression is a constant of motion even in case of a dissipative flow. If dissipation is absent ($\Delta Q = 0$), the above equation reduces to what is called the canonical form of Bernoulli constant and is given by,

$$\mathcal{E} = \frac{1}{2} v_{po}^2 + h + \Phi(r). \quad (21)$$

2.4 Relativistic EoS and the form of thermodynamic variables

We need an EoS which relates the thermodynamic variables. As discussed before, we used the relativistic EoS for multiple species flow with variable adiabatic indices given by [Chattopadhyay & Ryu \(CR\) in 2009](#). The form is given as follows,

$$e = \sum_i e_i = \sum_i \left[n_i m_i c^2 + p_i \left(\frac{9p_i + 3n_i m_i c^2}{3p_i + 2n_i m_i c^2} \right) \right], \quad (22)$$

where, n is the number density and index ‘ i ’ suggests a sum over the species that constitute the plasma. We have considered in our work a fully ionised plasma. Since, hydrogen is the most abundant element in the universe, an ionised flow is composed of electrons (e) and protons (p). We ignore in the present work the presence of pair production and its corresponding annihilation. Thus, the presence of positrons inside the system is negligible. We assume the plasma to be neutral, therefore $n_e = n_p$. On simplifying Eq. (22) using the expressions for n , ρ and p ([SCL20](#)) we get,

$$e = \rho_e c^2 \left(f_e + \frac{f_p}{\eta} \right) = \frac{\rho c^2 f}{\tilde{K}}, \quad (23)$$

where, $f_i = 1 + \Theta_i \left(\frac{9\Theta_i + 3}{3\Theta_i + 2} \right)$ and $f = f_e + f_p/\eta$. Here, $\eta = m_e/m_p$ and $\tilde{K} = 1 + 1/\eta$. $\Theta_e = kT_e/(m_e c^2)$ and $\Theta_p = kT_p/(m_p c^2)$ are dimensionless temperature of electron and proton respectively.

The adiabatic index for each species is self-consistently calculated from their temperature, using the following equation,

$$\Gamma_i = 1 + \frac{1}{N_i}, \quad (24)$$

where, $N_i = df_i/d\Theta_i$ is the polytropic index.

2.5 Final form of the equations of motion for two temperature flow

In the equations to follow, we drop all the subscripts ‘po’ which stands for poloidal components and represent the variables v_{po} with v , B_{po} with B , A_{po} with A and so on.

The differential equations for electron and proton temperatures are obtained by simplifying the first law of thermodynamics (Eq. 5) using Eq. 9 and the EoS (Eq. 22) to get:

$$\frac{d\Theta_e}{dr} = -\frac{\Theta_e}{N_e} \left[\frac{1}{v} \frac{dv}{dr} + \frac{3}{2r} \left(\frac{8-5r/r_d}{4-3r/r_d} \right) \right] - \mathbb{E}, \quad (25)$$

$$\frac{d\Theta_p}{dr} = -\frac{\Theta_p}{N_p} \left[\frac{1}{v} \frac{dv}{dr} + \frac{3}{2r} \left(\frac{8-5r/r_d}{4-3r/r_d} \right) \right] - \eta \mathbb{P}, \quad (26)$$

where, $\mathbb{E} = \Delta Q_e \tilde{K}/(\rho v N_e) (ds/dr)$ and $\mathbb{P} = \Delta Q_p \tilde{K}/(\rho v N_p) (ds/dr)$. The Q_i s used here are in dimensionless form which is derived from their dimensional counterparts \tilde{Q}_i (units of $\text{erg cm}^{-3} \text{s}^{-1}$) using the relation $\tilde{Q}_i r_s/(\tilde{\rho} c^3)$ where $\tilde{\rho}$ is the mass density of the species in units of g/cm^3 .

Simplifying Euler equation (Eq. 2) and substituting Eqs. 6–8, 14, 15, 19, 23–26, gives the gradient of poloidal velocity,

$$\frac{dv}{dr} = \frac{\mathcal{N}(r, v, \Theta_e, \Theta_p)}{\mathcal{D}(r, v, \Theta_e, \Theta_p)}, \quad (27)$$

where,

$$\mathcal{N} = \frac{3a_s^2}{2r} \left(\frac{8-5r/r_d}{4-3r/r_d} \right) + \frac{\mathbb{E} + \mathbb{P}}{\tilde{K}} - \Phi'$$

$$\mathcal{D} = v^2 \left(1 - \frac{a_s^2}{v^2} \right).$$

We have defined the speed of sound in two-temperature magnetized flow as, $a_s^2 = (\Gamma_e \Theta_e + \Gamma_p \Theta_p/\eta)/\tilde{K}$.

2.6 Emission processes

In this section, we discuss the radiative processes that are mainly responsible for the heating and cooling of protons and electrons present in the flow. Coulomb coupling is the main mechanism responsible for energy exchange between protons and electrons. It generally serves as a cooling term for protons and heating term for electrons. Therefore, $Q_p^- = Q_e^+ = Q_{cc}$. We assumed bremsstrahlung (Q_{br}) and synchrotron (Q_{syn}) as the main emission processes responsible for the cooling of electrons. The soft photons generated from these processes may upscatter to higher energies on interacting with energetic electrons through a process called inverse-Comptonization (Q_{cbr} and Q_{csy}). This radiative process leads to further cooling of electrons. Thus, $Q_e^- = Q_{br} + Q_{syn} + Q_{csy} + Q_{cbr}$. The seed photons generated by bremsstrahlung and synchrotron process can also heat up the electrons through a process called Compton heating ([Esin 1997](#)). This happens when the energy of the seed photons is greater than the thermal energy of the electrons present in the flow. This term (Q_{comp}) serves as a heating term for electrons rather than cooling. The expressions of all the above radiative processes have been given in [SC19a](#); [SC19b](#); [SCL20](#); [SC22](#) and references therein.

Black body emission and its Comptonization

Accreted matter on settling down onto the star’s poles can form a thermal mound. This optically thick mound is a source of blackbody photons which serves as an additional spectral component. These

soft photons on encountering electrons present in the post-shock accretion flow can get Comptonized. The formula used to calculate the height and temperature of the thermal mound is from [Becker & Wolff \(2007\)](#). We follow their prescription to obtain the corresponding emissivity and spectrum.

2.7 Spectral analysis

The methodology followed to obtain the spectrum as seen by a distant observer is similar to that as described in [Sarkar et al. \(2020\)](#); [Sarkar & Chattopadhyay \(2022\)](#) (also, see [Shapiro \(1973\)](#)). We briefly discuss it here. First we compute the emission, which is the isotropic emissivity per unit frequency per unit solid angle, in the fluid rest frame. This is represented by $j_\nu(r)$ and is computed at each radius of the flow. The unit is $\text{ergs s}^{-1} \text{cm}^{-3} \text{sterad}^{-1} \text{Hz}^{-1}$. The emissivity includes contribution from the different dissipative processes present inside the flow. Thus, $j_\nu = j_{\nu|\text{br}} + j_{\nu|\text{sy}} + j_{\nu|\text{cbr}} + j_{\nu|\text{csy}} + j_{\nu|\text{bb}} + j_{\nu|\text{cbb}}$. We use special-relativistic transformations to convert this j_ν from fluid rest frame to a local flat frame ($j'_{\nu'}$). The expressions for this transformation are given by:

$j'_{\nu'} = j_\nu \frac{1-v^2}{(1-v\cos\theta')^2}$ and $\nu' = \nu \frac{\sqrt{1-v^2}}{(1-v\cos\theta')}$. Here, θ' is the angle between the flow velocity (v) directed inwards towards the central object and the line of sight. On integrating the above expression for $j'_{\nu'}$ over the whole volume of the flux tube and on all solid angles we get the luminosity (L_ν) of the system per unit frequency interval. We have also included the effect of gravitational redshift which introduces a factor of $\sqrt{1-2/r}$ in the observed frequency. On integrating L_ν over all frequencies we get the bolometric luminosity. In this work we have presented the spectra in terms of $L_\nu/(h\nu)$ (in units of $\text{keV}^{-1} \text{s}^{-1}$) vs $h\nu$ (keV) for a better representation. We note here that the expressions of j_ν for bremsstrahlung, synchrotron and their respective Comptonizations have been taken from [Rybicki & Lightman \(1986\)](#); [Manmoto et al. \(1997\)](#); [Wardziński & Zdziarski \(2000\)](#). For computation of the emissivity of blackbody (BB) radiation from the thermal mound and its Comptonization we use the prescription followed by [Becker & Wolff \(2007\)](#) and [Shapiro & Salpeter \(1975\)](#). The amount of BB radiation depends on the height and width of the mound formed on the surface of the NS, the expressions of which are adopted from [Becker & Wolff \(2007\)](#).

2.8 Entropy accretion rate expression

Here we discuss and derive the entropy accretion rate formula for two-temperature accretion flows around magnetized stars. The derivation is exactly same as was in case of BHs ([SC19a](#); [SCL20](#)). Let us assume adiabaticity of protons and electrons and remove all the explicit heating and cooling terms present in the first law of thermodynamics (Eq. 5), which as discussed before is defined separately for electrons and protons in the two-temperature theory. Thus, we have,

$$\frac{d\Theta_p}{dr} = \frac{\Theta_p}{N_p} \frac{1}{n_p} \frac{dn_p}{dr} + \frac{Q_{cc}\eta\tilde{K}}{\rho\nu N_p}$$

and

$$\frac{d\Theta_e}{dr} = \frac{\Theta_e}{N_e} \frac{1}{n_e} \frac{dn_e}{dr} - \frac{Q_{cc}\tilde{K}}{\rho\nu N_e}. \quad (28)$$

This equation cannot be integrated analytically, due to the presence of Coulomb coupling term, unlike in case of one-temperature flows, where $T_p = T_e \Rightarrow Q_{cc} = 0$ and we have an analytical expression for entropy ([KSC18a](#); [KSC18b](#)).

However, it is possible to integrate Eq. (28) where Q_{cc} is 0 or negligible. This conjecture can only be fulfilled in regions where gravity dominates any other process or interaction. The strong gravity

implies that infall timescales in these regions would be shorter than any other timescales, such that before any dissipation processes act, the matter would be advected towards the central object. It is also in this region that adiabatic conditions are valid. Let at a distance r_{in} the flow approaches adiabatic condition. Thus, an analytical expression of entropy is obtained by integrating Eq. (28), using the adiabaticity condition and $Q_{cc} = 0$ at r_{in} and is given by,

$$n_{\text{ein}} = \tilde{\kappa}_1 \exp\left(\frac{f_{\text{ein}} - 1}{\Theta_{\text{ein}}}\right) \Theta_{\text{ein}}^{\frac{3}{2}} (3\Theta_{\text{ein}} + 2)^{\frac{3}{2}} \quad (29)$$

$$n_{\text{pin}} = \tilde{\kappa}_2 \exp\left(\frac{f_{\text{pin}} - 1}{\Theta_{\text{pin}}}\right) \Theta_{\text{pin}}^{\frac{3}{2}} (3\Theta_{\text{pin}} + 2)^{\frac{3}{2}}, \quad (30)$$

where, $\tilde{\kappa}_1$ and $\tilde{\kappa}_2$ are constants which measure entropy. Subscript 'in' defines quantities at r_{in} where the above assumptions hold true. Charge neutrality of the accretion flow suggests $n_{\text{ein}} = n_{\text{pin}} = n_{\text{in}}$. Therefore, we can write,

$$n_{\text{in}}^2 = n_{\text{ein}} n_{\text{pin}} \Rightarrow n_{\text{in}} = \sqrt{n_{\text{ein}} n_{\text{pin}}} \quad (31)$$

Thus,

$$n_{\text{in}} = \tilde{\kappa} \sqrt{\exp\left(\frac{f_{\text{ein}} - 1}{\Theta_{\text{ein}}}\right) \exp\left(\frac{f_{\text{pin}} - 1}{\Theta_{\text{pin}}}\right) \Theta_{\text{ein}}^{\frac{3}{2}} \Theta_{\text{pin}}^{\frac{3}{2}} (3\Theta_{\text{ein}} + 2)^{\frac{3}{2}} (3\Theta_{\text{pin}} + 2)^{\frac{3}{2}}}, \quad (32)$$

where, $\tilde{\kappa} = \sqrt{\tilde{\kappa}_1 \tilde{\kappa}_2}$.

Thus, the expression for entropy accretion rate, using Eq. (6), can be written as,

$$\begin{aligned} \dot{M}_{\text{in}} &= \frac{\dot{M}}{\tilde{\kappa}(m_e + m_p)} \\ &= \sqrt{\exp\left(\frac{f_{\text{ein}} - 1}{\Theta_{\text{ein}}}\right) \exp\left(\frac{f_{\text{pin}} - 1}{\Theta_{\text{pin}}}\right) \Theta_{\text{ein}}^{\frac{3}{2}} \Theta_{\text{pin}}^{\frac{3}{2}} (3\Theta_{\text{ein}} + 2)^{\frac{3}{2}}} \\ &\quad \times \sqrt{(3\Theta_{\text{pin}} + 2)^{\frac{3}{2}}} v_{\text{in}} A_{\text{in}}. \end{aligned} \quad (33)$$

This formula is exactly similar to what was obtained for BH accretion flows ([SC19a](#); [SCL20](#)). The importance and use of this formula in two-temperature flows around magnetized stars have been discussed briefly in section 3.

2.9 Sonic point conditions and shock conditions

Accretion flow around magnetized stars are generally transonic in nature, similar to flows around BHs ([Koldoba et al. 2002](#); [Karino et al. 2008](#); [KSC18a](#); [KSC18b](#)). The flow starts with a subsonic velocity, $v < a_s$ at $r \approx r_{\text{co}}$. As the matter gets accreted along the magnetic field lines the increase in gravitational potential energy of the matter leads to a corresponding increase in its kinetic energy. This increases the flow velocity. Additionally matter is also compressed to smaller and smaller volume as it gets accreted. Thus, as a secondary effect, the temperature and hence the sound speed increases. At a certain point of the flow r_c , the flow velocity is equal to the local sound speed $v_c = a_{sc} \Rightarrow$ or the Mach number at r_c , $M_c = 1$, where $M_c = v_c/a_{sc}$. This point is called the critical point of the flow. From Eq. (27), we see that when $v_c = a_{sc} \Rightarrow \mathcal{D} = 0$. For the flow to be smooth and continuous, \mathcal{N} should also go to 0. Thus, at r_c the velocity slope has the form, $dv/dr \rightarrow 0/0$. Now, because of the rotation of the star, a centrifugal force acts in opposite direction to gravity. This induces the formation of multiple critical (sonic) points (MCPs). The critical points are named according to the distance from the central object: inner (r_c^{in}), middle (r_c^{mid}) and outer (r_c^{out}). Out of these, r_c^{in} and r_c^{out} are X-type critical points and are physical

in nature, while r_c^{mid} is unphysical (spiral-type or O-type depending on whether the system is dissipative or not, respectively) and matter cannot flow through it. For X-type critical points, $dM/dr|_{r_c}$ possess two real roots: one < 0 , which corresponds to the accretion solution and the other > 0 , which is called the excretion solution. In the MCP regime an accretion flow can also harbour shocks. These shocks are called secondary shocks (r_{ss}) and are formed for certain combination of flow parameters, driven by the centrifugal and pressure gradient forces. These have been reported recently in the single temperature regime by [KSC18a](#); [KSC18b](#).

Apart from strong, ordered magnetic field of a magnetized star, the presence of a hard surface is an additional major difference, that distinguishes it from a BH. The accretion flow although accelerated to achieve transonicity by its strong gravity, has to settle down onto the star's surface. This drives a terminating shock, also known as primary shock (r_{ps}) (also see, [Fig. 1](#), dark maroon region). These are formed very close to the star's surface while secondary shocks are formed anywhere between the primary shock and the co-rotation radius (i.e., $r_{\text{ps}} < r_{\text{ss}} < r_{\text{co}}$). A primary shock is always formed and forces the flow to satisfy the star's surface boundary condition. However, secondary shocks are formed for a particular set of flow parameters.

In the strong magnetic field regime the MHD shock conditions ([Kennel et al. 1989](#)) reduce to hydrodynamic shock conditions ([KSC18a](#); [KSC18b](#)) and are given by,

$$\text{Conservation of mass flux : } [\rho v] = 0, \quad (34)$$

$$\text{Conservation of momentum flux : } [\rho v^2 + p] = 0, \quad (35)$$

$$\text{Conservation of energy flux : } [\dot{E}] = 0. \quad (36)$$

where the square brackets imply the difference between the pre-shock and post-shock flow variables.

3 METHODOLOGY

Here, we present first, the methodology to find general transonic two-temperature accretion solutions around strongly magnetized stars and then elaborately examine the problem of degeneracy present in two-temperature theory. After that, we discuss the use of entropy accretion rate formula given in section 2.8 to remove the degeneracy present in these type of solutions.

3.1 Methodology to obtain general two-temperature transonic solution around a strongly magnetized star

In this section we discuss the methodology to obtain general two-temperature accretion solutions onto a magnetised compact star, for a given set of CoM. But before going into the details it is important to remember that for a given set of CoM we will obtain multiple transonic solutions unlike in case of one-temperature flows where a unique solution is obtained ([KSC18a](#); [KSC18b](#)). The additional temperature variable in two-temperature regime and the absence of any equation relating this temperature with the other flow variables is responsible for the multiplicity of solutions. The entropy maximisation formulation which will be discussed in the upcoming section will serve as a tool to select only one solution out of all. Since the system we are working on is dissipative, we cannot have a measure of entropy and the entropy accretion rate form (Eq. 33) can only be used at a point r_{in} where the gravity is very strong and the matter velocities achieve free-fall velocity. Therefore, keeping in mind the importance of the point r_{in} we discuss here the methodology to find general solutions.

3.1.1 Utilising the property of gravity to find $r_{\text{in}} \rightarrow$ the inner boundary

The gravitational pull on any particle of unit mass by an object of mass M_* , depends on the value of M_* and also on the distance between the centre of gravities of these two masses. Utilising this property we can conclude that, if a star of mass M_* and radius r_* , is confined in a radius $r_{\text{in}} (< r_*)$, then the gravitational force experienced by a mass at a point r (where, $r > r_* > r_{\text{in}}$) would be exactly the same, irrespective of whether the radius of the star is r_* or r_{in} .

We find that it is at $r_{\text{in}} \rightarrow r_g$ that the infalling matter will asymptotically achieve free fall velocity and nowhere else. We select r_{in} as the inner boundary while obtaining solutions, assuming the star's mass to be concentrated within r_{in} . Once a solution is obtained, the portion of the solution within $r_{\text{in}} \leq r \leq r_*$ is called the ghost solution. We check for the terminating shock of the transonic solution in regions $r > r_*$.

In order to check whether this methodology to obtain solution works correctly, we obtain solutions in one temperature regime using this method (as described in section 3.1.2), and compare it with the solution obtained by [Singh & Chattopadhyay \(2018b\)](#), who used sonic point analysis method (see Appendix A). From the comparison of solutions in [Fig. A1](#), it is clear that both the methods are equivalent.

3.1.2 Steps to find a general TS or transonic solution

- (i) Supply the CoM (E, P, \dot{M}). Also, we need to supply surface magnetic field B_* of the magnetized star of mass M_* and radius r_* .
- (ii) We consider an inner boundary point $r_{\text{in}} \sim r_g < r_*$.
- (iii) We fix a value of Θ_{pin} at r_{in} . We note here that this is an extra variable present in two-temperature flows and was not present in one-temperature systems. Hence, before starting the methodology to find a global transonic solution (TS), we have to first fix a particular value of Θ_{pin} .
- (iv) We supply an initial guess value of Θ_{ein} at r_{in} .
- (v) We obtain the exact value of v_{in} , from the Bernoulli parameter expression obtained by equating of $E \equiv \mathcal{E}(v_{\text{in}}, \Theta_{\text{pin}}, \Theta_{\text{ein}})$ (Eq. 21).
- (vi) With the initial values of $v_{\text{in}}, \Theta_{\text{pin}}, \Theta_{\text{ein}}$ at r_{in} , we evaluate $dv/dr, d\Theta_p/dr$ and $d\Theta_e/dr$ (Eqs. 25-27) and then integrate these equations from $r = r_{\text{in}}$ outwards, with increasing r .
- (vii) There is a high probability that the guess value of Θ_{ein} might lead to a completely supersonic branch (SB) solution or a multi-valued branch (MVB) solution (similar to dotted blue curve or dashed dotted green of [Fig. A1b](#) in one-temperature case). So we iterate Θ_{ein} until the solution passes through a sonic point (r_c).
- (viii) Once r_c is found, $dv/dr|_{r_c}$ is obtained by employing L'Hospital's rule. Thereafter, we further integrate outwards till the co-rotation radius (r_{co}) is reached. In this way, we obtain the full global TS.
- (ix) It may be noted that there might be MCP for the same set of CoM and Θ_{pin} . For the same value of Θ_{pin} , which has produced a TS, we continue to search for other sonic points by changing the guess value of Θ_{ein} by a large factor and then repeating steps (iv)–(viii).
- (x) Once the TS is found, it needs to satisfy the star's surface boundary conditions. For every $r > r_*$ we impose a shock jump and using the corresponding subsonic post-shock values of the flow variables (obtained using Eqs. 34–36), we integrate the EoM inwards towards the star's surface until $r \rightarrow r_*$ is reached. We select the r for which the flow velocity at r_* reaches negligible values or the surface boundary conditions are satisfied ([Datta et al. 2021](#)). This is the primary shock location (r_{ps}).

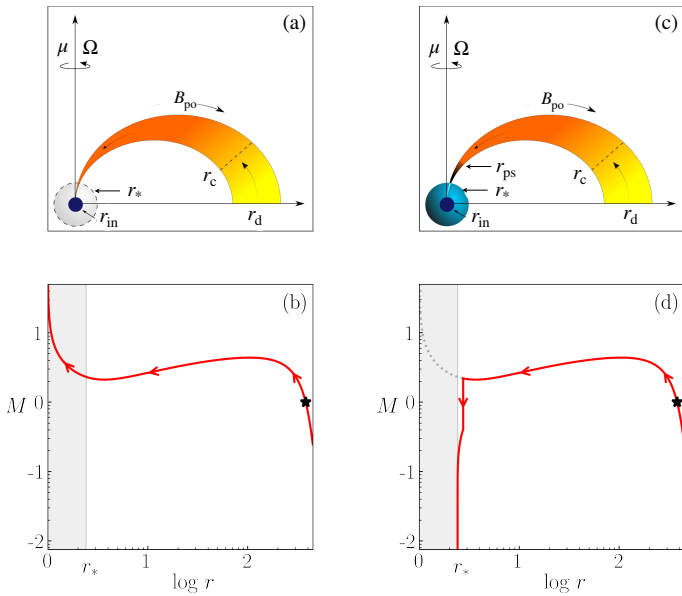


Figure 2. Panel (a) and (c) shows an accretion flow geometry where matter is accreted until it reaches a radius, $r_{\text{in}} \sim r_g (< r_*)$ and r_* respectively. In both cases the central object has a mass M_* . Panel (b) plots the TS solution corresponding to panel (a). When this flow satisfies the star’s surface boundary condition, the solution undergoes a primary shock transition near the surface and is plotted in panel (d). The ‘ghost solution’ is represented in dotted grey. The flow parameters are given in text below.

We note that throughout the aforementioned steps used for obtaining the TS, we have kept Θ_{pin} fixed. Thus, the global TS obtained can be identified using the value of Θ_{pin} apart from the supplied CoM. The above methodology is illustrated more elaborately in Figs. 2a–d. In Figs. 2a and c, cartoon diagram of an accretion flow around a magnetized star is presented. In Fig. 2a, the methodology to find the projected solution or the ghost solution is illustrated. The star surface r_* is presented in dashed circle and r_{in} is the supposed radius which contains the same mass $= M_*$ of the star but in a smaller volume. We consider $r_{\text{in}} \sim r_g$, so that $v \rightarrow$ free-fall. Figure. 2b plots the TS obtained following steps (i)–(ix), with the sonic point r_c represented by a black star. The flow parameters used for obtaining the solution are, $E = 0.9985$, $P = 1.16s$, $\dot{M} = 10^{15} \text{g/s}$, $B_* = 10^{10} \text{G}$, $M_* = 1.4M_\odot$ and $r_* = 10^6 \text{cm}$. The value of proton temperature at r_{in} for this solution is $T_{\text{pin}} = 1 \times 10^{11} \text{K}$ ($= \Theta_{\text{pin}} m_p c^2 / k$). Once the complete TS is obtained, one may find the location of the primary shock (r_{ps}), which is generally formed close to r_* . We represent the situation via a cartoon diagram in Fig. 2c, where after obtaining the full TS, the shock conditions were satisfied at $r_{\text{ps}} = 3.301r_g$ (dark maroon shade being the post-shock flow), see step (x).

In this way, we obtain a global two-temperature accretion solution around a magnetized star satisfying surface boundary conditions (see Fig. 2d).

3.2 Finding the unique two-temperature accretion solution: Problem of degeneracy and the methodology to constrain it

As have been discussed before, an increase in variable (an additional temperature) in two-temperature regime is not compensated with any increase in the number of equations or any additional relation, which relates it with the other flow variables at any boundary. The presence of an extra temperature variable is responsible for the degeneracy.

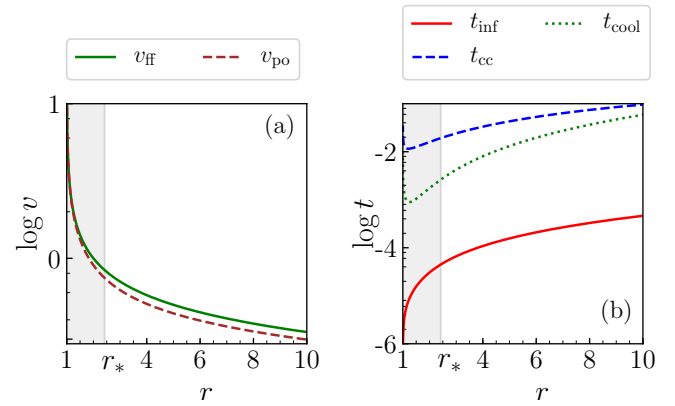


Figure 3. Comparison of (a) poloidal velocity (v_{po}) with free-fall velocity (v_{ff}) and (b) infall timescale (t_{inf}) with cooling (t_{cool}) and Coulomb coupling (t_{cc}) timescales.

This problem is generic in two-temperature theory and does not depend on the type of central object considered. We saw in step (iii) of the above section that Θ_{pin} was fixed for obtaining a particular global accretion solution, apart from the specified set of CoM. Keeping the CoM same, if Θ_{pin} is varied we would get a completely different global solution. This suggests that for a given set of CoM, we would get multiple accretion solutions each with different r_c and their properties. It can hence be concluded that two-temperature flows are degenerate in nature.

3.2.1 Entropy maximisation methodology in case of BHs

The problem was investigated in details by SC19a; SC19b; SCL20; SC22 for the case of two-temperature flows around BHs. Here, the degeneracy was constrained using the first principles, without taking recourse to any arbitrary assumption. In the absence of any physical principle constraining the relation between the temperatures, SC19a; SC19b; SCL20 utilised the concept of entropy to obtain a unique transonic two-temperature accretion solution. However, because of the presence of electron – proton energy exchange term or the Coulomb coupling term in the first law of thermodynamics, one cannot obtain an analytical expression for entropy measure. But it is known that near the BH horizon, strong gravity overwhelms any other interactions. Matter just outside the horizon falls freely and the infall timescales are shorter than cooling or Coulomb coupling time scales. Therefore, asymptotically close to the horizon, an analytical expression of entropy is admissible. Using this formula for entropy, strictly valid near the horizon, entropies of all the degenerate solutions were measured. It was found that the entropy maximised for a certain solution. Following the second law of thermodynamics, that nature would prefer a solution with maximum entropy, degeneracy was removed in two-temperature accretion flows around BHs. Additionally, it was shown that the maximum entropy solution is the most stable one (SCL20).

3.2.2 Entropy maximisation methodology in case of stars with hard surface

An inner boundary condition similar to BH is not present outside star’s surface. As discussed before, strong gravity of the magnetized star can make an accretion flow transonic, with matter approaching

the surface supersonically, however, the poloidal velocity of the supersonic branch is not high enough to approach free-fall values. To illustrate, we compare the poloidal velocity v_{po} (dashed brown) with the freefall velocity v_{ff} (solid green) in Fig. 3a for flow parameters $E = 0.9983$, $P = 1s$, $\dot{M} = 10^{15}g/s$, $M_* = 1.4M_{\odot}$, $r_* = 10^6cm$ and $B_* = 10^{10}G$. Certainly $v_{po} > v_{ff}$ everywhere, for $r > r_*$ (except at $r \rightarrow r_{in}$ where $v_{po} \rightarrow v_{ff}$, also see the discussion in Section 3.1.1). This is not very surprising, if we refer to Eq. 12. Free fall velocity is achieved when the first term on r. h. s (infall kinetic energy) is equal to gravitational energy (fourth term in r. h. s) and all other terms are negligible. Since other terms are present in the expression of E , then $v_{po} \ll v_{ff}$, except at $r \rightarrow r_{in}$, where gravity over powers all other interactions. Moreover, the presence of a hard surface intervenes the supersonic flow and drives a shock at r_{ps} near the surface and the accreting matter finally settles down with negligible velocities. In other words, neither the supersonic branch, nor the post shock flow achieves free-fall velocity. Therefore, one cannot obtain an entropy measure at the star's surface using the entropy formula given by Eq. 33, which is valid only in regions where infall velocity approaches free fall, i. e., where gravity over powers all other interactions. Thus, the methodology followed in case of BHs, cannot be adopted directly for flows around magnetized stars. Fortunately the methodology proposed in section 3.1.2 where r_{in} is used as the inner boundary solved the problem. Therefore, all the conditions needed to apply the entropy accretion rate formula (Eq. 33) are satisfied at r_{in} . Additionally in Fig. 3b, we show that infall timescale (solid red) in the funnel region is very much shorter than any other timescales (cooling or Coulomb coupling). It is the consequence of v_{po} being transonic along magnetic field line. Since infall time scale is much smaller than other relevant time scales, the accretion flow will be in the two-temperature regime.

Steps to constrain the degeneracy

The following steps needs to be implemented to constrain the degeneracy present in two-temperature accretion solutions around compact objects with a hard surface.

(xi) Once we have obtained the complete TS (following steps iii to ix) we note down the entropy measure (\dot{M}_{in}) at r_{in} using Eq. 33. We identify this entropy measure to the corresponding Θ_{pin} .

(xii) Now, keeping the CoM same, we change Θ_{pin} and repeat steps iii–ix. We obtain another TS and compute the corresponding \dot{M}_{in} . We carry out this process for different Θ_{pin} s. At the end, we will have a range of Θ_{pin} s and their corresponding \dot{M}_{in} s, all for the same set of CoM.

(xiii) Following the second law of thermodynamics, a unique accretion solution is the one which has the maximum entropy. Thus, we select that solution.

In Figs. 4a1–f1, we plot the TSs (solid curves) for different Θ_{pin} s (step xii). The flow parameters used are same as in Fig. 2. It is interesting to note that all these solutions are for the same set of CoM and hence we identify each solution using the corresponding value of Θ_{pin} . Their corresponding solutions which satisfy the surface boundary condition, are plotted in Figs. 4a2–f2. The dotted grey curve in each of these plots represent the ghost solutions. Values of T_{pin} used to obtain the different TS are, $1 \times 10^{11}K$ (Figs. 4a1, a2, red), $4.2 \times 10^{11}K$ (Figs. 4b1, b2, orange), $5.0 \times 10^{11}K$ (Figs. 4c1, c2, magenta), $6.0 \times 10^{11}K$ (Figs. 4d1, d2, blue), $7.0 \times 10^{11}K$ (Figs. 4e1, e2, green), and $7.2 \times 10^{11}K$ (Figs. 4f1, f2, brown). Solid curves represent the accretion solution, dotted lines represent the excretion

solution which is obtained because of the presence of two roots at $dv/dr|_{r_c}$ and dashed curves represent accretion solutions which are not global. Accretion solutions presented in Figs. 4a1, a2 and f1, f2, possess single sonic point, where it is outer type for the former (r_c^{out} marked with black star) and inner type for the later (r_c^{in} marked with black circle). Rest of the solutions presented in Figs. 4b1, b2–e1, e2, have MCPs (black stars and circles). There is also a centrifugal force driven shock transition in Figs. 4d1, d2, which is called a secondary shock (r_{ss}). The global solution in this case first passes through r_c^{out} , encounters a shock jump at r_{ss} and then again passes through r_c^{in} and then settles down onto the surface after encountering a terminal shock at r_{ps} .

It can hence be concluded that, by just varying the inner boundary values (Θ_{pin} at r_{in}) we obtain different topology of solutions, but all for the same set of CoM. But this should not be the case and a given set of CoM should necessarily harbour a unique solution. To remove this degeneracy we plot the entropy measure \dot{M}_{in} at r_{in} vs T_{pin} in Fig. 4g (step xi). The solid black curve represent entropies of solutions having outer sonic points and dashed is for solutions with inner sonic points. For few T_{pin} s both r_c^{in} and r_c^{out} exist. The coloured stars and circles correspond to \dot{M}_{in} s of TS plotted in Figs. 4a1, a2–f1, f2 (colour coding kept the same). \dot{M}_{in} is found to maximise for $T_{pin} = 4.2 \times 10^{11}K = T_{pin|max}$. The TS corresponding to $T_{pin|max}$ is plotted in Fig. 4b1 and after satisfying the surface boundary conditions, which is the final global accretion solution, is plotted in Fig. 4b2. Although this set of flow parameters and Θ_{pin} harbours multiple sonic point (orange star and orange circle), but due to the absence of a secondary shock transition the global accretion solution passes through r_c^{out} only (solid, orange).

Thus, to conclude, the maximum entropy solution is the one which nature would prefer. Following the second law of thermodynamics, we constrained the degeneracy (step xiii). As has been shown by SC19a; SC19b; SCL20; SC22 (but for the case of BH), among all the degenerate solutions the one with maximum entropy should be the unique accretion solution.

4 RESULTS

In this section we analyse in detail two temperature accretion flows around strongly magnetized compact stars in the presence of dissipative processes. We also perform their spectral analysis. The mass and radius of the compact star is assumed to be $M_* = 1.4M_{\odot}$ and $r_* = 10^6cm = 2.418r_g$, respectively throughout the paper, until otherwise mentioned. We chose the compact star parameters similar to a neutron star. All the solutions presented in the subsequent sections correspond to the maximum entropy solution and has been obtained using the methodology discussed above.

4.1 A typical two-temperature accretion solution around a magnetised compact star

We present a general two-temperature accretion solution in Fig. 5. The parameters used are, $E = 0.9986$, $P = 1.25s$, $\dot{M} = 10^{14}g/s$ and $B_* = 10^9G$. We plot flow variables in different panels which are: v (Fig. 5a), $\log B$ (Fig. 5b), $\log T_p$ and $\log T_e$ (Fig. 5c), $\log n$ (Fig. 5d), E (Fig. 5e) and Γ_p and Γ_e (Fig. 5f), all plotted as function of $\log r$. The location of sonic point, $r_c^{out} = 393.541r_g$ is marked with a black star and the location of the primary shock is at $r_{ps} = 3.035r_g$. In the post-shock region, enhanced density increases the cooling processes, which decreases the temperature as well as the velocity drastically. Moreover, the flow geometry (dictated by B , Eq. 15)

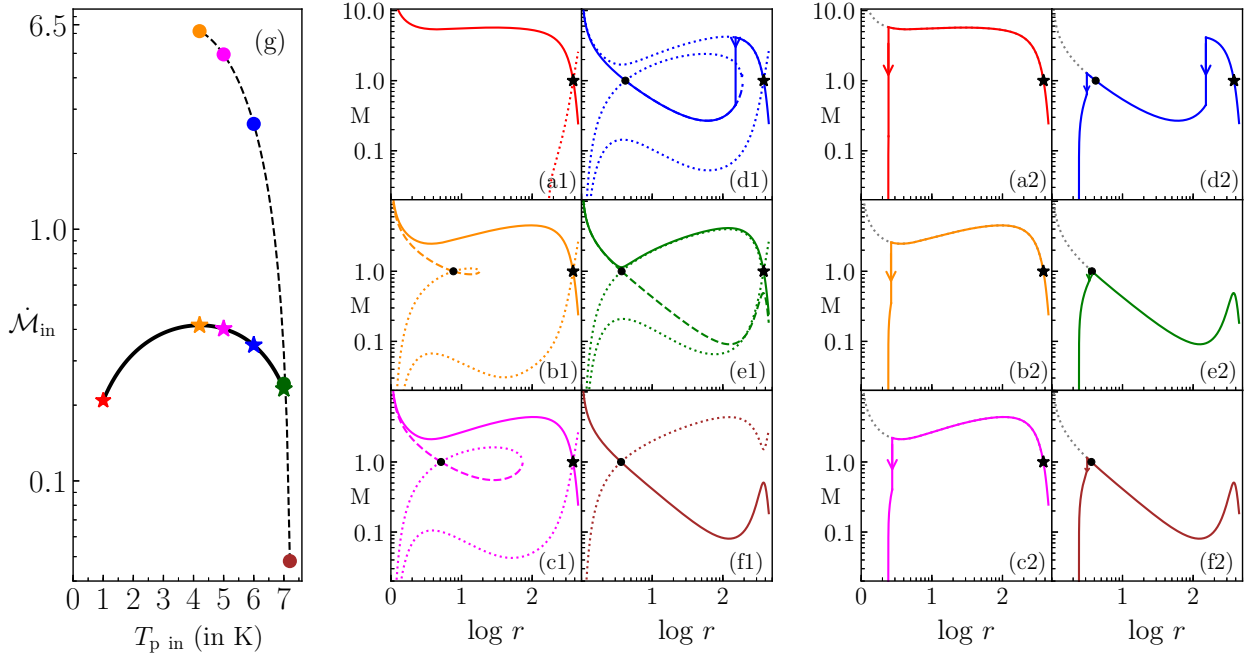


Figure 4. Methodology to remove degeneracy. Panels (a1–f1) plots the TS obtained using $r_{\text{in}} \sim r_{\text{g}}$ as inner boundary. Panels (a2–f2) plots the same solutions, after satisfying the surface boundary conditions at $r = r_*$. All the solutions presented are for the same set of CoM but corresponds to different T_{pin} s, values of which are 1.0×10^{11} K (red, panels a1, a2), 4.2×10^{11} K (orange, panels b1, b2), (c) 5.0×10^{11} K (magenta, panels c1, c2), (d) 6.0×10^{11} K (blue, panels d1, d2), (e) 7.0×10^{11} K (green, panels e1, e2) and (f) 7.2×10^{11} K (brown, panels f1, f2). The primary shock location (downward arrow), global (solid), excretion (dotted), non-global (dashed) and the ghost solutions (dotted grey), respectively are indicated accordingly. Panel (g) plots the entropy accretion rate values \dot{M}_{in} for all the values of T_{pin} possible: solid black curve represents solutions passing through r_c^{out} and dashed black is for solutions passing through r_c^{in} . Entropy is maximised at $T_{\text{pin}} = T_{\text{pin|max}} = 4.2 \times 10^{11}$ K. CoM used are same as in Fig. 2.

decreases faster than r^2 , which causes the n to increase sharply near the surface (Fig. 5d). The temperature of the species exhibits an interesting behaviour. T_{p} increases at the primary shock location due to shock heating, while, since the electrons primarily radiate, the enhanced density at the shock front causes T_e to dip at the primary shock location (Fig. 5c). The respective adiabatic indices follows the behaviour of the temperature distribution (Fig. 5f). The generalized Bernoulli parameter E , which is a constant of motion even in presence of dissipation is indeed found to be a constant (Fig. 5e).

Emissivities and spectrum

In Figs. 6a and b, we plot the emissivities and spectrum respectively, for different cooling mechanisms which are: bremsstrahlung Q_{br} (dotted, red), synchrotron Q_{syn} (dashed, blue), Comptonized bremsstrahlung Q_{cbr} (dashed single-dotted, magenta) and Comptonized synchrotron Q_{csy} (dashed double-dotted, green). Matter accreted through the magnetic funnels on settling down onto the poles of the NS may form a thermal mound. This thermal mound is a source of black-body photons of emissivity Q_{bb} (dashed four-dotted, brown), which on encountering with hot electrons can get Comptonized, whose emissivity is represented by Q_{cbb} (dashed triple-dotted, orange). The total emission from all these processes combined, is shown by solid black line. The flow parameters are same as that in Fig. 5. We find that Q_{br} dominates in the pre-shock region. As soon as the flow encounters primary shock, emission from all the processes increase due to the increase in number density of the system (see, Fig. 5d). After the primary shock, Q_{csy} dominates over all other emission processes. But very near the surface, Q_{br} and Q_{cbr} dominate because of

the rapid increase in n . Also in this region, there is reduction in synchrotron and its Comptonized emission because of the decrease in T_e due to the increased cooling. The total luminosity of this system is $L = 2.759 \times 10^{34}$ erg s $^{-1}$. Contribution of individual emission processes to the total luminosity are: bremsstrahlung= 6.909×10^{32} erg s $^{-1}$, synchrotron= 5.567×10^{30} erg s $^{-1}$, Comptonized synchrotron= 1.589×10^{34} erg s $^{-1}$, Comptonized bremsstrahlung= 1.100×10^{34} erg s $^{-1}$ and Comptonized blackbody= 2.052×10^{30} erg s $^{-1}$.

In Fig. 6b, we represent the spectrum in terms of $L_{\nu}/(h\nu)$ (in units of s $^{-1}$ keV $^{-1}$) vs $h\nu$ (in keV). It is apparent from the figure, that bremsstrahlung emission contributes from radio to gamma rays: covering the whole electromagnetic spectrum, but it mainly dominates upto near-infrared frequencies. A hump in optical and near UV regime is contributed by synchrotron emission. A power law of spectral index $\alpha = 0.365$, covering from UV to X-rays is because of Comptonized synchrotron. A second hump is formed in the gamma ray region which is contributed by Comptonized bremsstrahlung. Blackbody emission from the thermal mound at the NS surface is represented by dashed four-dotted brown line and contributes mainly in the low energy part, while its Comptonized component represented by dashed triple-dotted orange line, contributes in the UV and soft X-rays.

4.2 Contribution of different regions of an accretion flow in the emitted spectrum

In Fig. 7 we examine the contribution of different regions of an NS accretion flow to the observed spectrum. The flow parameters are $E = 0.9985$, $P = 1.15$ s and $\dot{M} = 10^{15}$ g/s, with surface magnetic

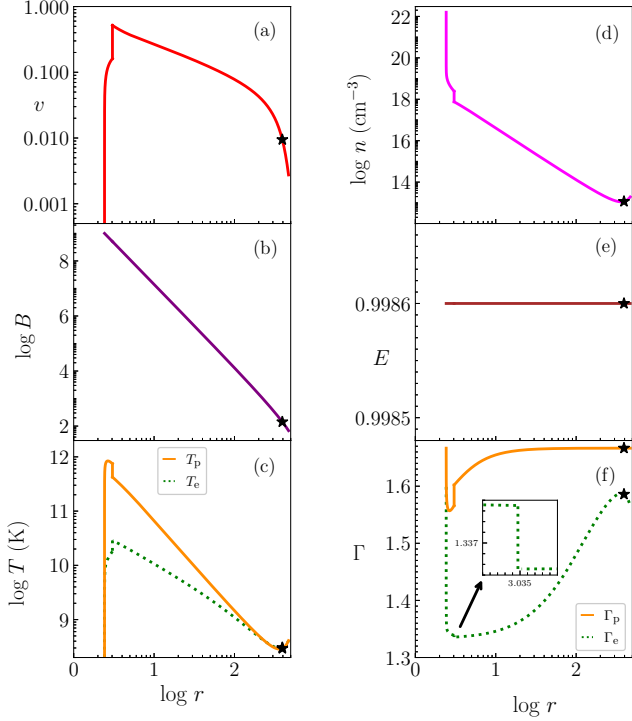


Figure 5. Flow variables corresponding to a typical two-temperature accretion solution around a compact star are plotted. The flow parameters are, $E = 0.9986$, $P = 1.25s$, $\dot{M} = 10^{14}g/s$ and $B_* = 10^9G$. For these parameters there is only one sonic point (r_c^{out}) marked with a black star.

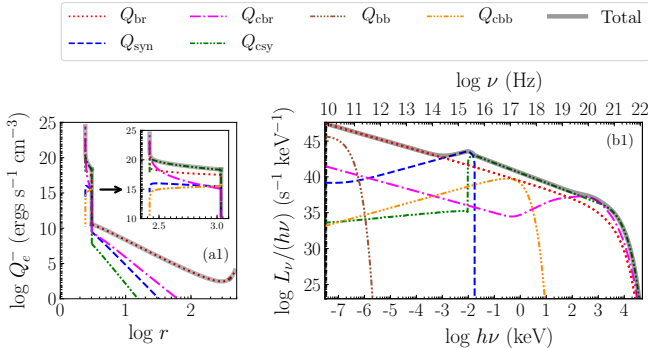


Figure 6. (a) Emissivities (Q_e^-) and (b) corresponding spectrum ($L_\nu/(h\nu)$ vs $h\nu$) are plotted. Parameters used are same as in Fig. 5.

field, $B_* = 5 \times 10^9G$. In Fig. 7a, we plot M vs $\log r$. The global accretion solution passes through $r_c^{out} = 375.720r_g$ (black star), which encounters a primary shock at $r_{ps} = 2.829r_g$ (downward black arrow) which is of strength $S = M_-/M_+ = 6.082$ and compression ratio $CR_{ps} = n_+/n_- = 4.571$. Profile of T_e (solid, orange) and T_p (dotted, magenta) are plotted in Fig. 7b left Y-axis and n (dashed, dark-blue) is plotted in right Y-axis. In Fig. 7a, we have divided the solution into six different regions (shaded with different colours). The regions are as follows: $2.418r_g (= r_*) - 2.829r_g$ (brown), $2.829r_g - 5r_g$ (violet), $5r_g - 7r_g$ (blue), $7r_g - 10r_g$ (green), $10r_g - 100r_g$ (yellow) and $100r_g - 444.810r_g$ (red). The spectrum from these regions are plotted respectively in Figs. 7c1–c6 following the same colour coding,

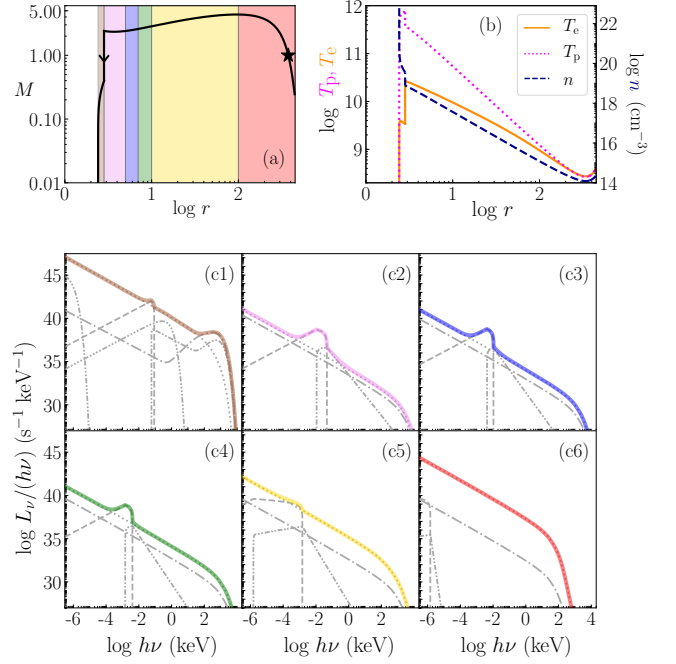


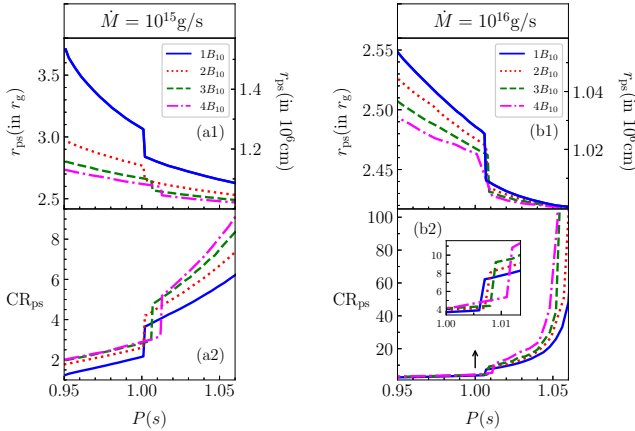
Figure 7. (a) Accretion solution (solid, black) is plotted. Different regions have been marked, which are: $2.418r_g - 2.829r_g$ (brown), $2.829r_g - 5r_g$ (violet), $5r_g - 7r_g$ (blue), $7r_g - 10r_g$ (green), $10r_g - 100r_g$ (yellow) and $100r_g - 444.810r_g$ (red). (b) Variation of T_e (solid, orange), T_p (dotted, magenta) and n (dashed, dark-blue) are plotted. Spectral contribution of different regions marked in panel (a) have been correspondingly plotted in solid curves in panels (c1–c6), using the same colour coding. In each of these panels, contribution from different emission processes are represented in grey. The flow parameters used are, $E = 0.9985$, $P = 1.15s$, $\dot{M} = 10^{15}g/s$ and $B_* = 5 \times 10^9G$.

in solid curves. In each of these panels, spectral contribution from different radiative processes are plotted in grey: Q_{br} (dotted), Q_{syn} (dashed), Q_{cbr} (dashed single-dotted), Q_{csy} (dashed double-dotted), Q_{bb} (dashed four-dotted) and Q_{cbb} (dashed triple-dotted). The total bolometric luminosity of the system is $L = 2.376 \times 10^{35} \text{ erg s}^{-1}$. We have tabulated the contributions of each region in table 2.

The existence of an NS hard surface causes the flow to come to a halt at r_* . This, combined with the effect of number density jump at r_{ps} , increases the cooling processes to such an extent, that most of the radiation comes from the post-shock region (Fig. 7c1). At r_{ps} , temperatures should generally increase due to compression of matter at the shock front, but the excessive radiative cooling causes T_e to drop to a lower value. Unlike electrons, protons cannot radiate efficiently. Thus, T_p follows the general trend as expected in a shock transition and jumps to a higher value. Conforming to the above arguments, we find that the post-shock region is very bright, with 99.99985% of the total luminosity (L_{tot}) contributed from this region. Contribution from Comptonized components decrease and becomes negligible for regions $> 10r_g$. Similarly, the hump which is a signature of synchrotron emission, decrease and vanish for $r > 100r_g$. This is due to the decrease in B with increase in radius (Eq. 15). Also, synchrotron self-absorption peak frequency (ν_t), decrease to lower energies, shifting from EUV in panel (c1) to optical in panel (c4). In regions $> 10r_g$, the total emission is mainly contributed from bremsstrahlung. It may be noted that, since we are adding up large sections of accretion flow in the last two panels c5: $10r_g - 100r_g$ and

Table 2. Radiative properties of the regions shaded in Fig. 7

Panel No.	Colour	Region (in r_g)	L (erg s^{-1})	% of L_{tot}
c1	Brown	2.418 – 2.829	2.376×10^{35}	99.99985
c2	Violet	2.829 – 5.0	1.158×10^{28}	4.875×10^{-6}
c3	Blue	5.0 – 7.0	5.567×10^{27}	2.343×10^{-6}
c4	Green	7.0 – 10.0	4.796×10^{27}	2.018×10^{-6}
c5	Yellow	10.0 – 100.0	1.586×10^{28}	6.676×10^{-6}
c6	Red	100.0 – 444.810	3.221×10^{29}	1.355×10^{-4}

**Figure 8.** Primary shock location r_{ps} (a1, b1) and compression ratio CR_{ps} (a2, b2) as function of P are plotted for two different \dot{M} : 10^{15} g/s (a1, a2) and 10^{16} g/s (b1, b2). In each panel there are four curves, representing four B_* values, where B_{10} represents magnetic field in units of 10^{10} G. $E = 0.9984$ is fixed for all cases.

c6: $100r_g - 444.810r_g$, the amount of emission is higher compared to regions presented in panels c3 and c4.

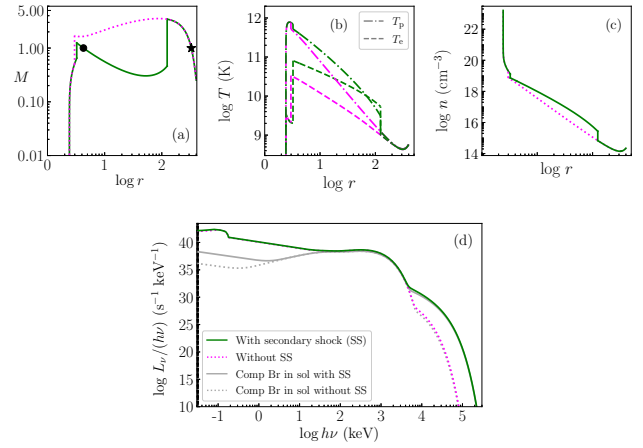
4.3 Shock analysis

In this section, we examine the properties of primary as well as secondary shocks and their spectral signatures.

4.3.1 Properties of primary shock

A primary shock is necessary to slow down the matter such that the surface boundary conditions can be satisfied. This slowing down happens because of dissipative or cooling processes, which in turn is responsible for most of the emission coming from an NS. In the last section, we concluded that majority of the emission comes from the post-shock region. We now investigate the variation of primary shock location (r_{ps}) (Figs. 8a1, b1) and compression ratio (CR_{ps}) (Figs. 8a2, b2) with P as well as B_* of the NS. We used four different values of B_* : B_{10} (solid, blue), $2B_{10}$ (dotted, red), $3B_{10}$ (dashed, green) and $4B_{10}$ (dashed-dotted, magenta), where B_{10} represents magnetic field in units of 10^{10} G. We also use two different values of accretion rate for this purpose, $\dot{M} = 10^{15}$ g/s (Figs. 8a1, a2) and $\dot{M} = 10^{16}$ g/s (Figs. 8b1, b2). The specific energy has been fixed to 0.9984 for all cases.

Shorter P implies faster spin, so the rotational energy enhances the resistance to the inflowing supersonic matter. As a result r_{ps} form at larger distances. This trend is irrespective of the magnitude of B_* and \dot{M} , and is apparent from Figs. 8a1, b1. In these plots, the left

**Figure 9.** Comparison of accretion solutions, with (solid, green) and without secondary shock transition (dotted, magenta). Plotted in panel (a) M vs $\log r$, where solid black circle and black star represents r_{c}^{in} and $r_{\text{c}}^{\text{out}}$ respectively; (b) T_{p} (dashed dotted) and T_{e} (dashed) (green is for solution with two shocks, magenta is for solution harbouring only a primary shock); (c) $\log n$; (d) comparison of continuum spectra along with the Comptonized bremsstrahlung components plotted in grey, with the same linestyle as the solutions. The flow parameters are, $E = 0.9984$, $P = 0.98$ s, $\dot{M} = 10^{15}$ g/s and $B_* = 10^{10}$ G.

Y-axis represents the shock location in terms of r_g and the right Y-axis represents it in terms of $r_* = 10^6$ cm, which is the NS radius. At larger distance from the NS surface, the thermal energy and therefore the pressure is lower. As a result, CR_{ps} is lower too (see, Figs. 8a2, b2). It may be noted that with the increase in B_* , synchrotron and its Comptonization increases which in turn reduces the thermal energy. As a result, for a given P , increase in B_* decrease r_{ps} and increase CR_{ps} . Because of the same reason, r_{ps} is formed nearer to the NS surface for solutions with higher accretion rate (see Fig. 8b1) as compared to the corresponding lower accretion rate solutions (see Fig. 8a1). Since these primary shocks are formed near to the surface, the CR_{ps} s have very high values, especially when the rotation period is higher along with B_* value. This is seen in Fig. 8b2.

In Figs. 8a1, b1, a2, b2, as the rotation period is increased, a sudden drop appears near $P \sim 1.0$ s. This is due to the change in topology of global accretion solutions as we change the rotation period. For lower rotation periods (fast spin), matter becomes supersonic on passing through r_{c}^{in} , while for higher rotation periods, matter crosses $r_{\text{c}}^{\text{out}}$ and become supersonic. The period P where this transition of accretion flow occurs from r_{c}^{in} to $r_{\text{c}}^{\text{out}}$, r_{ps} is found to drop to a lower value. The location of this drop depends on the combination of flow parameters used.

4.3.2 Properties of secondary shock

Now we study the importance of secondary shock in accretion flows around NS and discuss the necessity to obtain a global transonic solution which connects the matter from the accretion disc to NS poles. We present in Fig. 9a an accretion solution along with its other flow variables in Fig. 9b (T_{e} and T_{p}) and Fig. 9c (n). We also plot the spectrum in Fig. 9d. The flow parameters are, $E = 0.9984$, $P = 0.98$ s, $\dot{M} = 10^{15}$ g/s and $B_* = 10^{10}$ G. The solution passes through $r_{\text{c}}^{\text{out}}$ (marked using a black star) and becomes supersonic, which is shown in Fig. 9a. Centrifugal and pressure gradient forces oppose this supersonic matter which drives a shock at $r_{\text{ss}} = 124.074r_g$. This is termed as a secondary shock (SS). The post-shock subsonic flow

then picks up speed due to the gravity of NS and again becomes supersonic at r_c^{in} (black circle). This supersonic flow finally encounters the hard surface of the NS and as a result settles on it after passing through a primary shock at $r_{\text{ps}} = 3.247r_g$. Accretion solution which passes through these two shock locations: r_{ps} and r_{ss} , is presented using a solid, green curve in Fig. 9a. Suppose, we do not check for the Rankine-Hugoniot shock conditions (Eqs. 34–36) for regions $r < r_c^{\text{out}}$, then the flow will remain supersonic until it reaches near the NS surface, where it will encounter only a primary shock at $r_{\text{ps}} = 2.976r_g$. This flow is represented using dotted, magenta line. It is clear that the two solutions are quite different. In Fig. 9b, we compare the corresponding temperature distributions of both the electron population T_e (dashed) and the proton population T_p (dashed dotted) of the accretion solution with two shocks (green) and with only a single primary shock (magenta). Solution which does not harbour the secondary shock (dotted, magenta) is found to be much colder. Hence, r_{ps} for this solution is formed closer to the NS surface, where the thermal pressure is large. T_e at r_{ps} for both the solutions decreases, while at r_{ss} , it increases. This is because, in the post-shock flow of r_{ss} , the velocity start to increase just after the initial downward jump at the shock front. This reduces the infall time scales, thereby prohibiting the post-shock flow to loose enough energy through cooling. In case of primary shock, the velocity decrease at the shock front similar to r_{ss} , but it also steadily decrease afterwards until it reaches the NS surface, where it finally settles down. Infall timescales in these cases become larger, allowing matter to radiate more. Therefore after r_{ps} , T_e gradually decreases. The radiative processes are not significant in case of proton gas, and thus its temperature increases in the post-shock region irrespective of whether it is a primary or secondary shock. From the number density distribution in Fig. 9c, it is clear that the solution with two shocks (solid, green) is denser compared to the solution with only a primary shock (dotted, magenta). In Fig. 9d, we compare the continuum spectra of accretion flows with two-shocks (solid, green) and the solution with only primary shock (dotted, magenta). We plot in grey, the corresponding Comptonized bremsstrahlung components, keeping the same linestyle. The solution which harbours secondary shock as argued before, is hotter and much denser. Apart from that, the secondary shock is also quite strong. Because of all these reasons, the high energy tail of the spectrum extends beyond 10^5 keV, most of the emission being contributed from the enhanced Comptonized bremsstrahlung post r_{ss} . This extra high energy component obtained in gamma rays is a signature that a secondary shock exist.

In Fig. 10 we did a similar study as Fig. 8 but this time it is for secondary shocks. Unlike primary shocks, secondary shocks are formed for a certain combination of flow parameters and are generally located far away from the star’s surface, as is apparent from the values presented in Figs. 10a1, b1. For any given B_* , the shock location decreases with increasing P (slow spinning) and therefore the compression ratio CR_{ss} increases. This is similar to what was observed in case of primary shocks (see, Fig. 8a1, b1). The centrifugal force decreases, which causes the shock to move towards the surface. For a given value of P , r_{ss} increase with B_* , thereby decreasing CR_{ss} . Similar effect occurs when the accretion rate is increased. It may be noted that even though compression ratio of the secondary shock is less than the primary shock, but the secondary shock by itself is quite strong.

4.4 Effect of magnetic field and spin period on the solution

In this section, we study the change in solution topology and the observable spectra in Figs. 11 and 12 respectively for varying surface

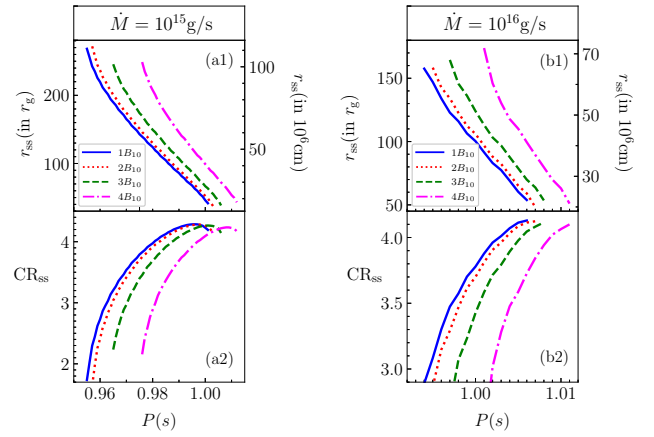


Figure 10. Secondary shock location r_{ss} (a1, b1) and compression ratio CR_{ss} (a2, b2) as function of period P are plotted for two different accretion rates 10^{15} g/s (a1, a2) and 10^{16} g/s (b1, b2). In each panel there are four curves, representing four B_* values, where B_{10} represents magnetic field in units of 10^{10} G . $E = 0.9984$ for all cases.

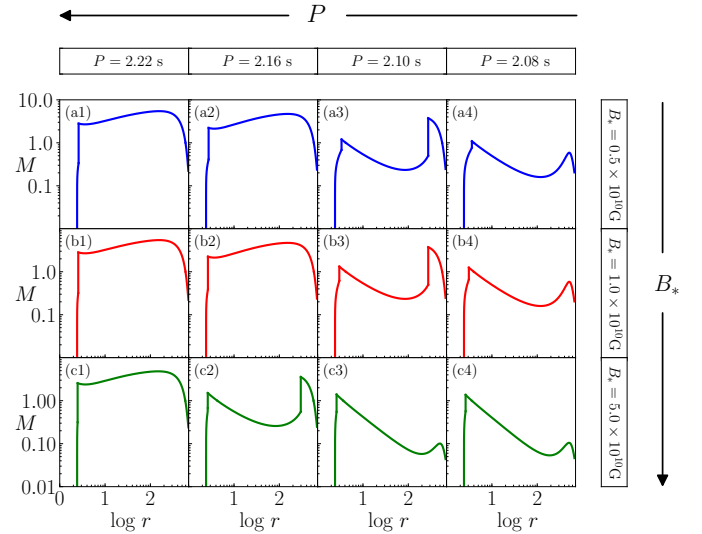


Figure 11. Plot showing the variation of solutions with change in B_* (top to bottom) and P (left to right) of the NS. Other flow parameters are $E = 0.999$ and $\dot{M} = 10^{15} \text{ g/s}$.

magnetic field values (B_*) and rotation periods (P) of the NS system. In both the figures, P decrease from left to right with values 2.22s, 2.16s, 2.10s and 2.08s, labelled as 1–4, while B_* increase on going from top to the bottom, with values: $0.5 \times 10^{10} \text{ G}$, $1.0 \times 10^{10} \text{ G}$ and $5.0 \times 10^{10} \text{ G}$ and labelled as a–c. Rest of the parameters are $E = 0.999$ and $\dot{M} = 10^{15} \text{ g/s}$. For high spin period or slowly rotating magnetized star, e.g. $P = 2.22\text{s}$ (Figs. 11a1, b1, c1), rotational energy is low, therefore the accretion solution possess only one outer type sonic point or r_c^{out} . However, for fast rotating NS or spin period like $P = 2.08\text{s}$ (Figs. 11a4, b4, c4), the rotational energy is quite high, such that the accretion flow can become supersonic ($M > 1$) only very close to the star’s surface, i.e., possess only r_c^{in} . For intermediate values of P , solutions would harbour secondary shocks (Figs. 11a3, b3, c2).

Fixing B_* , if P is varied, we see that for low values of B_* like

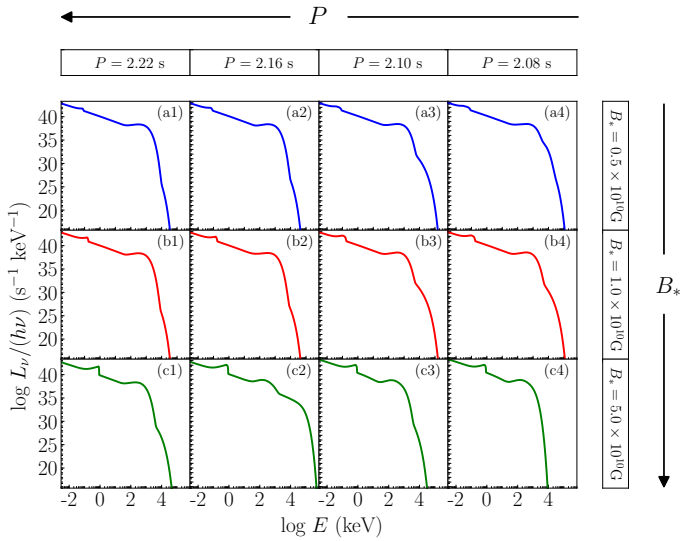


Figure 12. Plot showing the corresponding change in observable spectra with change in B_* and P of the NS. Parameters used are same as in Fig. 11.

0.5×10^{10} G and 1.0×10^{10} G, secondary shock can be formed for fast rotating NS, $P = 2.10$ s, where centrifugal force is large (see Figs. 11a3, b3). However for higher magnetic fields $B_* = 5 \times 10^{10}$ G, they can be found even for slow rotating NS, $P = 2.16$ s (Fig. 11c2). This is because, B determines the flow geometry or in other words, the flux tube thickness. This affects n , which in turn influence v and T_e . Also, the synchrotron cooling and its Comptonization depends on the value of B . Redistribution of the flow variables trigger shock transition.

The corresponding continuum spectra for the flows presented in Fig. 11 are given in Fig. 12. Bolometric luminosity (L) increases with decrease in P . A fast spinning NS would restrict the infalling matter, allowing it to radiate for a longer duration. But with increase in B_* for a given P , L decreases. It may be remembered that $> 99\%$ of total luminosity comes from the region between r_* and r_{ps} and for higher B_* , post-shock T_e is smaller. Therefore, the total luminosity is less for flows with higher B_* . Moreover, flows with higher B_* produce a prominent synchrotron self-absorption peak, which shift to higher energies with increase in B_* . Interestingly, the combination of P and B_* which admits secondary shocks (Figs. 11a3, b3, c2; and 12a3, b3, c2), exhibits extended high energy tail and high energy cut-offs ($> 10^5$ keV) similar to Fig. 9d. Extensive discussion about this feature has already been done in Section 4.3.2.

It may be noted that we did not consider very high magnetic field ($\geq 10^{11}$ G) in Figs. 11 & 12. Recently Kluzniak & Lasota (2015) inferred a dipole magnetic field strength of $\sim 10^9$ G for M82 X-2. Also, King et al. (2017); King & Lasota (2019, 2020) inferred from their model that pulsating ultra-luminous X-ray sources having NSs as their central objects, have dipole magnetic field strengths of the order of $10^9 - 10^{13}$ G, with majority falling between 10^{10} and 10^{11} G (Abarca et al. 2021). The magnetic field ranges in these systems are similar to most of the cases that have been discussed in the current work. To briefly see the effect of higher magnetic field on accretion flows we consider two NSs, one with surface magnetic field 10^{11} G and another with 10^{12} G and plot their spectrum in Fig. 13, keeping all other flow parameters same. As expected, higher surface magnetic field systems creates a more luminous accretion column with a harder spectra in the higher energies.

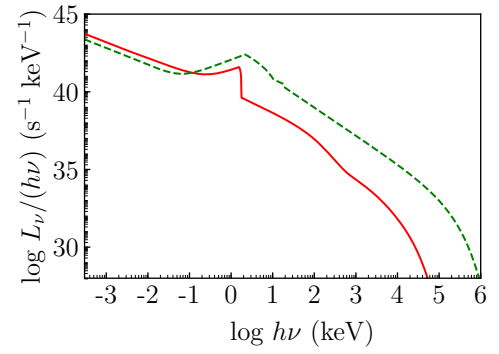


Figure 13. Comparing the spectra for two surface magnetic field configuration $B_* = 10^{11}$ G (solid, red) and 10^{12} G (dashed, green). Flow parameters are, $P = 5.1$ s, $\dot{M} = 10^{15}$ g/s and $E = 0.999$.

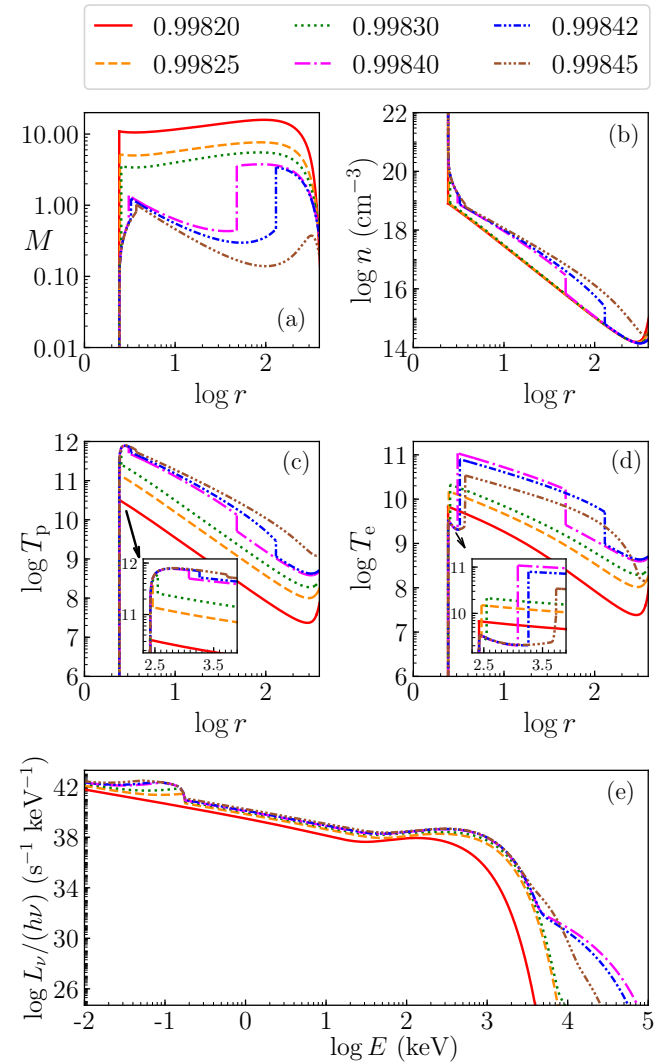


Figure 14. Effect of variation of E on different accretion flow variables and continuum spectra are presented. Different values of E are in the legend. Flow parameters are, $P = 1.0$ s, $\dot{M} = 10^{15}$ g/s and $B_* = 10^{10}$ G.

Table 3. The effect of variation of E on solutions plotted in Fig. 14

E	Primary shock		Secondary shock		L (erg s ⁻¹) ×10 ³⁵
	r_{ps}	CR _{ps}	r_{ss}	CR _{ss}	
0.99820	2.419	229.896	–	–	0.068
0.99825	2.461	16.628	–	–	0.922
0.99830	2.548	8.736	–	–	1.595
0.99840	3.079	2.128	47.888	4.244	2.769
0.99842	3.260	1.748	129.522	3.950	2.915
0.99845	3.732	1.207	–	–	3.114

4.5 Effect of Bernoulli parameter (E)

In Fig. 14, we analyse the effect of Bernoulli parameter on accretion flows around NS. We plot in panel (a) M , (b) $\log T_p$, (c) $\log T_e$, (d) $\log n$ and (e) continuum spectra. Each curve inside these panels, correspond to different values of E : 0.99820 (solid, red), 0.99825 (dotted, orange), 0.99830 (dashed, green), 0.9984 (dashed single-dotted, magenta), 0.99842 (dashed double-dotted, blue) and 0.99845 (dashed triple-dotted, brown). Other flow parameters are, $P = 1.0s$, $\dot{M} = 10^{15} \text{g/s}$ and $B_* = 10^{10} \text{G}$. Higher E implies higher temperature distribution (i.e., higher a_s). Therefore, matter becomes supersonic ($v > a_s$) after it is accelerated to a much higher infall velocity by gravity, i.e., the sonic point moves inward. This is seen in case of $E = 0.99845$ (dashed triple-dotted, brown) where the accretion flow has single r_c^{in} . For low E , the accretion flow has one r_c^{out} . This is found for $E = 0.99820$ (solid, red), 0.99825 (dotted, orange) and 0.99830 (dashed, green). For intermediate values of E , MCPs may exist, which allows for the formation of secondary shocks ($E = 0.9984$, dashed single-dotted, magenta and $E = 0.99842$, dashed double-dotted, blue). r_{ss} will be formed at a large distance for higher E , because of higher thermal energy. Generally T_p is higher for higher E (Fig. 14b), while T_e is highest for energies which harbour secondary shocks (Fig. 14c). In Fig. 14d, variation in n is presented which shows that it increases with increase in E . When an accretion flow harbour secondary shock, there is a distinct density jump seen at the shock front. This leads to enhanced cooling, which is responsible for the appearance of a prominent high energy tail (dashed single-dotted, magenta and dashed double-dotted, blue curves in Fig. 14e). But this does not increase the bolometric luminosity substantially since $r_{ss} \gg r_{ps}$ and it is already known that most of the luminosity is contributed from regions $< r_{ps}$. However, the L increase with increase in E . In table 3, we summarize the effect of variation of E on accretion flows around NSs. We list the values of r_{ps} and r_{ss} (if any), their CRs and the corresponding L .

4.6 Effect of variation of accretion rate

In Fig. 15 each panel, we plot the variation in number density (n) along a flux tube represented in two dimensional X-Y plane. The number density values, in units of cm^{-3} , are presented using a colour bar. The different panels show system with different \dot{M} : (a) $1.0 \times 10^{15} \text{g/s}$, (b) $5 \times 10^{15} \text{g/s}$, (c) $9.8 \times 10^{15} \text{g/s}$, (d) $1.0 \times 10^{16} \text{g/s}$, (e) $1.2 \times 10^{16} \text{g/s}$ and (f) $2.5 \times 10^{16} \text{g/s}$. The other flow parameters are, $E = 0.9983$, $P = 0.91s$ and $B_* = 8 \times 10^9 \text{G}$. n increases with increase in \dot{M} . However, due to strong magnetic field assumption, the flux tube width is independent of the \dot{M} value, which is apparent from the figure. In Figs. 15a, b, the flow passes through one r_c^{out} . With increase in \dot{M} , accreting matter becomes hotter, increasing thermal pressure and as a result secondary shock appear, which is seen in Figs. 15c–e. In the inset of each panel, we zoomed the region around primary and secondary shocks. The location of secondary shock (r_{ss}) for panels c–e

are, $38.131r_g$, $40.848r_g$ and $56.426r_g$, respectively, while r_{ps} values for panels a–f are, $2.928r_g$, $2.526r_g$, $2.493r_g$, $2.491r_g$, $2.470r_g$ and $2.428r_g$, respectively. If we further increase the accretion rate of the system, then the flow passes through a single inner sonic point (r_c^{in}), which is formed very close to the NS surface. This is seen for accretion rate $2.5 \times 10^{16} \text{g/s}$ (Fig. 15f). All these solutions harbour primary shock irrespective of the presence of any secondary shock.

Spectra corresponding to Fig. 15 are plotted in corresponding panels of Fig. 16. The luminosity increases with increase in accretion rate of the system. A prominent synchrotron turnover frequency is observed around 0.1keV for $\dot{M} = 1.0 \times 10^{15} \text{g/s}$ (see, Fig. 16a). Its magnitude and location remains almost the same irrespective of \dot{M} , because, ν_t depends strongly on the value of B . But this signature subsides with increasing \dot{M} of the system. It is mildly visible for $5 \times 10^{15} \text{g/s}$ (see, Fig. 16b). For a given magnetic field structure, increasing \dot{M} , increases n and thereby bremsstrahlung emission and its Comptonization. Therefore, for higher \dot{M} systems, the synchrotron turn over frequency is masked by the dominance of bremsstrahlung emission. For solutions harbouring secondary shock, there is an extended power law, with the cut-off going to higher energies similar to the spectra discussed in sections before.

5 DISCUSSIONS AND CONCLUSIONS

In this paper we investigated two-temperature accretion flows around strongly magnetized stars specifically NSs.

The major impediment for obtaining self-consistent two-temperature solution is that, the transonic solution is not unique. The total number of governing equations are less than the total number of flow variables to be computed. This problem is same as that observed for two-temperature flows around BHs. To conclude, the degeneracy in two-temperature regime is generic in nature and is irrespective of the type of central object. For a given set of constants of motion, infinite transonic solutions are admissible. The problem of degeneracy around BHs were solved by computing the entropy of the flow very close to the event horizon and then choosing the solution with the maximum entropy. It may be noted that, for two-temperature flows there is no analytical expression for entropy. But an entropy measure form can be derived only very close to a point where the accreting matter approach free-fall velocity. However, such a situation is not possible on or outside the surface of a magnetized star. Therefore, in this paper we proposed a novel method to obtain a unique transonic two-temperature accretion solution around a strongly magnetized star. By strong field, we only meant that we chose a surface magnetic field of the star, such that the magnetic energy density is much stronger than the gas energy density, so the magnetic fields are not deformed due to the gas motion and the flow remains sub-Alfvénic. We traced the projected transonic solution, assuming the star to be more compact, to a point $r_{\text{in}} \sim r_g$ such that the infall velocities at this radius is found to approach free-fall values. Obtaining all possible solutions for a given set of CoM or constants of motion, we chose the highest entropy solution following the second law of thermodynamics. This is the unique solution. It may further be noted that the highest entropy solution at r_{in} will remain the highest entropy solution at r_d . Even if the flow at r_d starts with arbitrary T_e and T_p the solution will be time-dependent until it achieve values which will correspond to those having highest entropy. Somewhat similar argument can be extended for Bondi flows (Bondi 1952), where, in presence of all non-transonic solutions as well as a transonic solution, the flow would choose the highest entropy transonic global solution only.

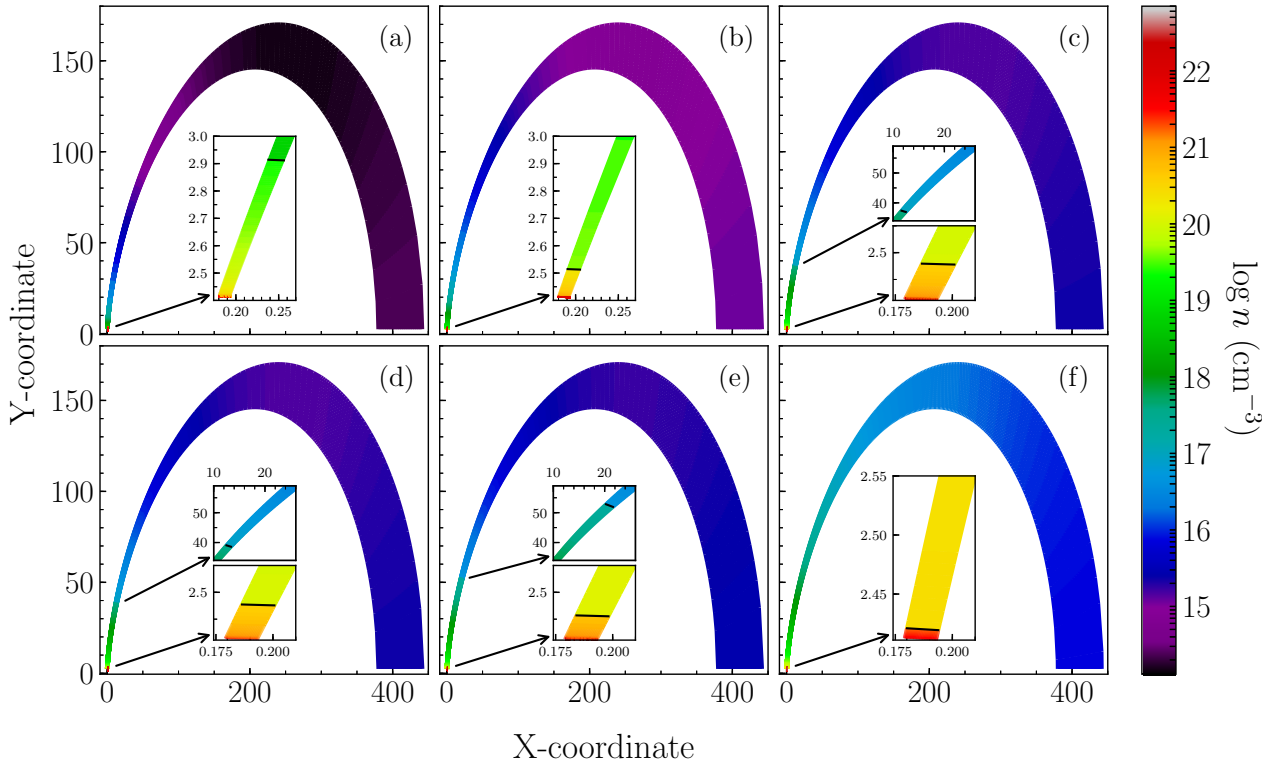


Figure 15. The variation of number density (n) inside a flux tube represented in two spatial dimension. The different panels correspond to systems with different \dot{M} : (a) 1.0×10^{15} g/s, (b) 5×10^{15} g/s, (c) 9.8×10^{15} g/s, (d) 1.0×10^{16} g/s, (e) 1.2×10^{16} g/s and (f) 2.5×10^{16} g/s. Other parameters are $E = 0.9983$, $P = 0.91s$ and $B_* = 8 \times 10^9$ G.

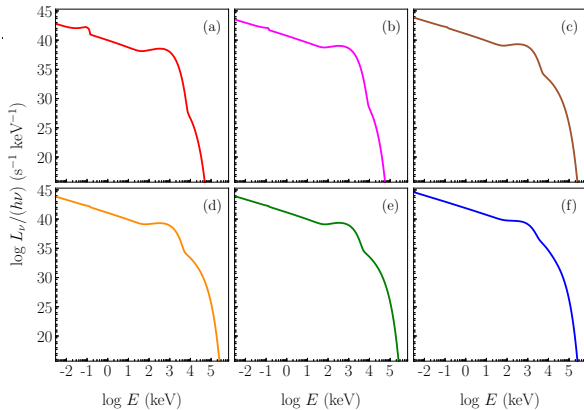


Figure 16. Spectra corresponding to the flows presented in Fig. 15.

After proposing a general methodology to constrain degeneracy, we investigated two-temperature accretion solutions around NS for a wide range of parameter space. There are accretion solutions which become supersonic after passing through an outer sonic point, while others become supersonic after passing through the inner sonic point. There are even solutions which passes through outer sonic point and suffers a secondary shock, after which it becomes subsonic. Thereafter, this solution becomes supersonic after passing through the inner sonic point. All these solutions have one thing in common i. e., all these solutions ends up with a terminating shock at the NS surface. This shock ensures that the surface boundary conditions are

satisfied. We found that almost the entire radiation is emitted from this post-shock flow. The secondary shock, thus, do not significantly influence the total luminosity, however it is responsible for an additional high energy tail or an extended high energy cut-off. So, there is a need to study the accretions solutions connecting the accretion disc to the NS poles, and not just investigate the radiative property of a freely falling accretion column onto a NS.

The compression ratio across the primary shocks are very high and depend on the combination of flow parameters used. Secondary shocks, on the other hand, have compression ratios less than that of primary shocks, but strength of these shocks are not very low. Apart from adding high energy tail via inverse-Comptonization of soft photons, such shocks can also aid in particle acceleration. Presence of high density and very low speed, makes the electron temperature distribution decrease at the primary shock location, due to enhanced cooling, contrary to what is expected at a shock front.

The combination of flow parameters present in an NS is important in determining the flow topology and the observable spectrum. Apart from the thermal Comptonization mechanisms considered in this paper, there could be bulk motion Comptonization present in the system as well (Becker & Wolf 2005a, 2007). An order of magnitude estimate of this emission process has been conducted. And we arrived at the conclusion that the accretion rates we have considered, radiation from the mound would not exert any significant resistance and would not change the qualitative nature of the solutions presented. A detailed discussion on this process is beyond the scope of this paper and will be dealt with properly in our future works.

DATA AVAILABILITY

The data underlying this article will be shared on reasonable request to the corresponding author.

REFERENCES

- Abarca D., Parfrey K., Kluźniak W., 2021, *ApJ*, 917, L31
 Arons J., Klein R. I., Lea S. M., 1987, *ApJ*, 312, 666
 Becker P. A., 1998, *ApJ*, 498, 790
 Becker P. A., Le T., 2003, *ApJ*, 588, 408
 Becker P. A., Wolff M. T., 2005a, *ApJ*, 621, L45
 Becker P. A., Wolff M. T., 2005b, *ApJ*, 630, 465
 Becker P. A., Wolff M. T., 2007, *ApJ*, 654, 435
 Becker P. A., Wolff M., 2020, in American Astronomical Society Meeting Abstracts #235. p. 408.02
 Becker P. A., Wolff M. T., 2022, arXiv e-prints, p. arXiv:2211.13894
 Becker P. A., Das S., Le T., 2008, *ApJ*, 677, L93
 Becker P. A., et al., 2012, *A&A*, 544, A123
 Biryukov A., Abolmasov P., 2021, *Monthly Notices of the Royal Astronomical Society*, 505
 Bondi H., 1952, *MNRAS*, 112, 195
 Bu D.-F., Qiao E., Yang X.-H., 2020, *The Astrophysical Journal*, 890, 116
 Chael A., Narayan R., Johnson M. D., 2019, *Mon. Not. Roy. Astron. Soc.*, 486, 2873
 Chandrasekhar S., 1939, An introduction to the study of stellar structure
 Chandrasekhar S., 1956, *ApJ*, 124, 232
 Chattopadhyay I., Ryu D., 2009, *ApJ*, 694, 492
 Colpi M., Maraschi L., Treves A., 1984, *ApJ*, 280, 319
 Datta S. R., Dhang P., Mishra B., 2021, *ApJ*, 918, 87
 Davidson K., 1973, *Nature Physical Science*, 246, 1
 Davidson K., Ostriker J. P., 1973, *ApJ*, 179, 585
 Dihingia I. K., Das S., Mandal S., 2018, *MNRAS*, 475, 2164
 Dihingia I. K., Das S., Prabhakar G., Mandal S., 2020, *MNRAS*, 496, 3043
 Esin A. A., 1997, *ApJ*, 482, 400
 Fukue J., 1987, *PASJ*, 39, 309
 Giacconi R., Gursky H., Kellogg E., Schreier E., Tananbaum H., 1971, *ApJ*, 167, L67
 Heinemann M., Olbert S., 1978, *Journal of Geophysical Research: Space Physics*, 83, 2457
 Karino S., Kino M., Miller J. C., 2008, *Progress of Theoretical Physics*, 119, 739
 Kennel C. F., Blandford R. D., Coppi B., 1989, *Journal of Plasma Physics*, 42, 299
 King A., Lasota J.-P., 2019, *MNRAS*, 485, 3588
 King A., Lasota J.-P., 2020, *MNRAS*, 494, 3611
 King A., Lasota J.-P., Kluźniak W., 2017, *MNRAS*, 468, L59
 Kluźniak W., Lasota J. P., 2015, *MNRAS*, 448, L43
 Koldoba A. V., Lovelace R. V. E., Ustyugova G. V., Romanova M. M., 2002, *AJ*, 123, 2019
 Lamb F. K., Pethick C. J., Pines D., 1973, *ApJ*, 184, 271
 Langer S. H., Rappaport S., 1982, *ApJ*, 257, 733
 Li J., Wickramasinghe D. T., Ruediger G., 1996, *ApJ*, 469, 765
 Liang E. P. T., Thompson K. A., 1980, *ApJ*, 240, 271
 Lovelace R. V. E., Mehanian C., Mobarry C. M., Sulkanen M. E., 1986, *ApJS*, 62, 1
 Lyne A. G., Manchester R. N., 1988, *MNRAS*, 234, 477
 Mandal S., Chakrabarti S. K., 2005, *A&A*, 434, 839
 Manmoto T., Mineshige S., Kusunose M., 1997, *ApJ*, 489, 791
 Medvedev M. V., Narayan R., 2001, *ApJ*, 554, 1255
 Mestel L., 1968, *MNRAS*, 138, 359
 Nakamura K. E., Matsumoto R., Kusunose M., Kato S., 1996, *PASJ*, 48, 761
 Narayan R., Yi I., 1995, *ApJ*, 452, 710
 Paczyński B., Wiita P. J., 1980, *A&A*, 500, 203
 Park M.-G., 1990, *ApJ*, 354, 83
 Pringle J. E., Rees M. J., 1972, *A&A*, 21, 1
 Rybicki G. B., Lightman A. P., 1986, *Radiative Processes in Astrophysics*

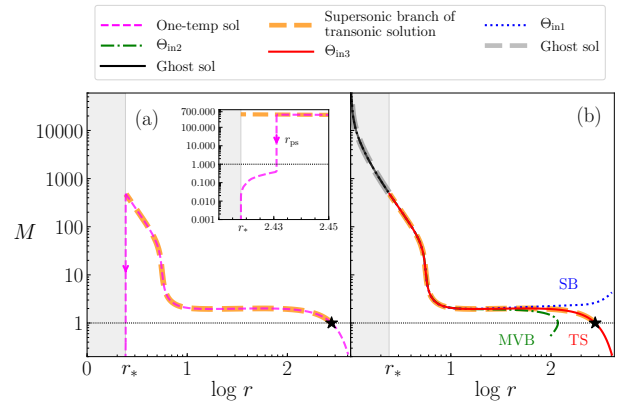


Figure A1. (a) One-temperature solution (dashed, magenta) obtained by sonic point analysis of accretion flows around an NS (KSC18b). The primary shock (r_{ps}) is shown using downward arrow (see zoomed inset). Thick dashed orange curve marks just the supersonic branch of this solution. (b) Obtaining solutions with r_{in} as the inner boundary. TS (solid, red) obtained completely coincides with dashed magenta/thick dashed orange curve. The solid black and thick dashed grey lines are part of the TS below r_* and are named as the ghost solutions. The location of primary shock remains the same. The input parameters used are, $E = 0.9977$, $P = 1.0s$, $\dot{M} = 2.957 \times 10^{15} \text{g/s}$, $B_* = 10^{10} \text{G}$, $M_* = 1.4M_{\odot}$ and $r_* = 10^6 \text{cm} = 2.418r_g$.

- Ryu D., Chattopadhyay I., Choi E., 2006, *ApJS*, 166, 410
 Sarkar S., Chattopadhyay I., 2019a, *International Journal of Modern Physics D*, 28, 1950037
 Sarkar S., Chattopadhyay I., 2019b, in *Journal of Physics Conference Series*, p. 012019, doi:10.1088/1742-6596/1336/1/012019
 Sarkar S., Chattopadhyay I., 2022, *Journal of Astrophysics and Astronomy*, 43, 34
 Sarkar S., Chattopadhyay I., Laurent P., 2020, *A&A*, 642, A209
 Saxton C. J., Wu K., Cropper M., Ramsay G., 2005, *MNRAS*, 360, 1091
 Shapiro S. L., 1973, *ApJ*, 180, 531
 Shapiro S. L., Salpeter E. E., 1975, *ApJ*, 198, 671
 Shapiro S. L., Lightman A. P., Eardley D. M., 1976, *ApJ*, 204, 187
 Singh K., Chattopadhyay I., 2018a, *Journal of Astrophysics and Astronomy*, 39, 10
 Singh K., Chattopadhyay I., 2018b, *MNRAS*, 476, 4123
 Sądowski A., Wielgus M., Narayan R., Abarca D., McKinney J. C., Chael A., 2017, *Mon. Not. Roy. Astron. Soc.*, 466, 705
 Stepney S., 1983, *MNRAS*, 202, 467
 Sądowski A., Wielgus M., Narayan R., Abarca D., McKinney J. C., Chael A., 2016, *Monthly Notices of the Royal Astronomical Society*, 466, 705
 Taub A. H., 1948, *Physical Review*, 74, 328
 Ustyugova G. V., Koldoba A. V., Romanova M. M., Chechetkin V. M., Lovelace R. V. E., 1999, *ApJ*, 516, 221
 Wardziński G., Zdziarski A. A., 2000, *MNRAS*, 314, 183
 Weber E. J., Davis Leverett J., 1967, *ApJ*, 148, 217
 West B. F., Wolfram K. D., Becker P. A., 2017a, *ApJ*, 835, 129
 West B. F., Wolfram K. D., Becker P. A., 2017b, *ApJ*, 835, 130
 Wolff M., et al., 2019, *BAAS*, 51, 386
 Yang H.-R., Li X.-D., 2023, *J. 10.48550/arXiv.2302.11243*
 Yuan F., Narayan R., 2014, *ARA&A*, 52, 529
 Yuan F., Quataert E., Narayan R., 2003, *ApJ*, 598, 301

APPENDIX A: REGENERATING ONE-TEMPERATURE ACCRETION SOLUTION AROUND A STRONGLY MAGNETIZED STAR USING THE NEW METHODOLOGY PROPOSED IN THIS PAPER

In the one-temperature regime, for a given set of CoM E , P and \dot{M} , a transonic solution is unique. Therefore, one can solve it using different methodologies but every method will admit a unique solution. In this section, we show that our proposed ‘ghost solution’ method indeed regenerates the same accretion solution as was obtained by [KSC18b](#), who started the integration from the critical point.

In Fig. A1a, a typical one-temperature transonic accretion solution onto an NS is presented, which has been obtained following the methodology of [KSC18b](#). Here, M is plotted against radial distance (r) from the center of the NS. The parameters used are, $E = 0.9977$, $P = 1.0s$, $\dot{M} = 2.957 \times 10^{15} \text{g/s}$, surface magnetic field $B_* = 10^{10} \text{G}$ and $M_* = 1.4M_\odot$. Radius of the NS, $r_* = 10^6 \text{cm} = 2.418r_g$, is marked in the figure and region below it is shaded in grey. The global transonic solution (hereafter, abbreviated as TS) (satisfying NS boundary condition) is represented by dashed magenta curve with the sonic point r_c , marked using a black star. The star surface drives a primary shock (downward magenta arrow) at r_{ps} , located just near the surface (see, zoomed inset plot), after which matter becomes subsonic and then slowly settles down onto the star ($v \rightarrow 0$ at $r \rightarrow r_*$). If the matter would have directly hit the surface of the star without undergoing the primary shock transition, the supersonic branch in such a case would be the one which is marked using a thick dashed orange line. The cooling processes considered are same as those present in [KSC18b](#). The methodology adopted by these authors to obtain an accretion solution is the general ‘sonic point analysis’ method. In this method, given a set of constants of motion, the location of r_c is found first. Then from r_c , the equations of motion are integrated inwards (till the star’s surface: to obtain the supersonic branch; thick dashed orange curve) and outwards (till r_{co} : to obtain the subsonic branch). Now, at every radius of the supersonic branch (especially in the region near the star’s surface), they check for the allowed shock transitions until the post-shock branch satisfies the surface boundary condition ([Datta et al. 2021](#)). In this way, the location of r_{ps} is found and a global TS including surface shock is obtained.

In Fig. A1b, we compare this TS (dashed, magenta) with the ‘ghost solution method’ proposed in this paper. We consider a point at $r_{in} \sim r_g$ where the gravity is very strong such that any other interaction or processes can be considered negligible. Then, for the same set of CoM as before (Fig. A1a), we supply a guess value of $\Theta = \Theta_{in1}$ at r_{in} . We estimate $v_{in1} [\equiv v_{in}(E, \dot{M}, \Theta_{in1})]$, equation obtained from the canonical form of Bernoulli parameter] and integrate out from r_{in} , using the EoM. Suppose for Θ_{in1} we obtain a completely supersonic branch (SB, dotted blue) of solution. This branch of solution is not physical. Hence, in the next iteration we change the guess value of Θ_{in} to Θ_{in2} and correspondingly estimating the value of v_{in2} , we obtain another solution. We might obtain a multi-valued branch (MVB, dashed dotted green) of solution which too is unphysical. Hence, we iterate in between these two Θ_{in} values until for say Θ_{in3} we get a TS (solid, red). We can see from Fig. A1b, that this solution completely masks the underlying dashed magenta curve, but the thick dashed orange supersonic branch bears the witness that the two transonic curves have coincided with each other. Portion of the TS (solid, red) inside the grey shaded region, represented using black curve, is the ‘ghost solution’ or the ‘projected transonic solution’. This is actually a continuation of the TS obtained by [KSC18b](#), i.e. when the supersonic branch obtained by sonic point analysis method (thick

dashed orange) is integrated further inwards till r_{in} is reached and is not terminated at the NS surface (r_*), then the solution obtained below r_* (thick dashed grey) overlaps with the black curve. The location of primary shock remains the same for both these methods. Thus, using the ‘ghost solution’ method, we have regenerated the full transonic solution as was obtained by [KSC18b](#).

Hence, we conclude that the new proposed method just uses the property of gravity, that is, it behaves as if the mass is concentrated at the centre and therefore the ‘ghost solution’ is actually a part of the full solution, only to be chopped off by the boundary condition. This method in brief, directs us to obtain the projected transonic accretion solution, by starting the integration from a region smaller than the actual star surface.

This paper has been typeset from a $\text{\TeX}/\text{\LaTeX}$ file prepared by the author.